NASA TECHNICAL NOTE

NASA TN D-4080

NASA TN D-4080

EFFECTS OF CONFIGURATION MODIFICATIONS ON AERODYNAMIC CHARACTERISTICS OF TENSION SHELL SHAPES AT MACH 3.0

by James Wayne Sawyer and William D. Deveikis

Langley Research Center

Langley Station, Hampton, Va.

NATIONAL AERONAUTICS AND SPACE ADMINISTRATION • WASHINGTON, D. C. • AUGUST 1967

NASA TN D-4080

EFFECTS OF CONFIGURATION MODIFICATIONS ON AERODYNAMIC CHARACTERISTICS OF TENSION SHELL SHAPES AT MACH 3.0

By James Wayne Sawyer and William D. Deveikis

Langley Research Center
Langley Station, Hampton, Va.

NATIONAL AERONAUTICS AND SPACE ADMINISTRATION

For sale by the Clearinghouse for Federal Scientific and Technical Information
Springfield, Virginia 22151 – CFSTI price $3.00

EFFECTS OF CONFIGURATION MODIFICATIONS ON AERODYNAMIC CHARACTERISTICS OF TENSION SHELL SHAPES AT MACH 3.0

By James Wayne Sawyer and William D. Deveikis
Langley Research Center

SUMMARY

An investigation was conducted at a Mach number of 3.0 to determine the effectiveness of configuration modifications applied at the base of tension shell-shaped models in delaying the onset of flow separation and thus improving the resultant aerodynamic characteristics. Three configurations were modified by systematically reducing the base radius in 5-percent increments to 80 percent of the original radius while maintaining a corner radius at the base of either 0 or 5 percent of the original base radius. The tests were conducted at angles of attack from 0° to 12° and at Reynolds numbers, based on maximum base diameter, of approximately 1.0×10^6 and 3.0×10^6. Reducing the base radius and increasing the corner radius delayed flow separation to higher angles of attack and significantly improved static stability. However, the modifications also caused a loss in drag coefficient.

INTRODUCTION

In the investigation of reference 1 on aerodynamic characteristics of tension shell shapes, a number of high-drag configurations encountered boundary-layer separation at low angles of attack and also exhibited poor static stability. The flow separation was accompanied by abrupt changes in the static forces and moments with attendant loss of drag. The configurations were bodies of revolution with negative Gaussian curvature such as illustrated in figure 1. A positive pressure gradient along the flow path renders such shapes susceptible to flow separation.

The present investigation was undertaken to explore the effectiveness of configuration modifications designed to induce flow attachment and thus maintain a steady, relatively high drag capability over a greater angle-of-attack range. The configurations were modified by systematically reducing the base radius while maintaining a corner radius at the base of either 0 or 5 percent of the original base radius. (See fig. 2.) The modifications were applied to three configurations selected from those of reference 1. One configuration was pointed and had encountered leeward flow separation at an angle

of attack of 9° but had attached flow at 0° angle of attack. The other two configurations were spherically blunted and had encountered extensive flow separation at 0° angle of attack.

Aerodynamic force tests were conducted at angles of attack from 0° to 12°. Free-stream Mach number was 3.0, and Reynolds numbers, based on original model base diameter, were approximately 1.0×10^6 and 3.0×10^6.

SYMBOLS

The units used for the physical quantities defined in this paper are given in the U.S. Customary Units and in the International System of Units (SI) (ref. 2). Factors relating the two systems are given in appendix A.

A^2 shape parameter associated with Newtonian pressure (see ref. 3)

A_b model base area, $\pi(r_b')^2$

C_A axial-force coefficient, $\frac{\text{Axial force}}{qA_b}$

C_D drag coefficient, $\frac{\text{Drag force}}{qA_b}$

C_m pitching-moment coefficient, $\frac{\text{Pitching moment}}{2qA_b r_b'}$

$C_{m_\alpha} = \frac{\partial C_m}{\partial \alpha}$ at $\alpha = 0°$, per degree

C_N normal-force coefficient, $\frac{\text{Normal force}}{qA_b}$

$C_{N_\alpha} = \frac{\partial C_N}{\partial \alpha}$ at $\alpha = 0°$, per degree

l model length (fig. 2)

M free-stream Mach number

N_θ, N_φ circumferential and meridional stress, respectively

q dynamic pressure

R Reynolds number based on original model base diameter

r radial coordinate

r_b original model base radius

r_b' reduced model base radius

r_c upstream corner radius at model base

r_n spherical nose radius

x axial coordinate (fig. 2)

x_{cp} axial coordinate of center of pressure

α angle of attack, degrees

β angle between body axis and tangent to surface at nose juncture, degrees

β_o nose semivertex angle for $r_n = 0$, degrees

δ flow turning angle, degrees

MODELS, APPARATUS, AND TESTS

Models

Three basic shapes of the type shown in figure 2 were tested. Two of the shapes were derived from membrane theory and Newtonian pressure distribution (ref. 3) to give a ratio of circumferential-to-meridional stress N_θ/N_φ of zero. One of these shapes had a pointed tip and the other was spherically blunted such that $r_n/r_b = 0.10$. The nose semivertex angle β_o for these shapes was 27.0^o. The third shape was derived for the condition that $N_\theta/N_\varphi = 0.15$ and was also spherically blunted such that $r_n/r_b = 0.218$. The angle β at the spherical cap juncture was 23.5^o. All shapes were modified by reducing the base radius in increments of 5 percent of the original base radius until $r_b'/r_b = 0.80$, as shown in figure 2. The flow turning angle δ corresponding to each base radius varied from 90^o to approximately 56^o for the $N_\theta/N_\varphi = 0$ shapes and from 90^o to approximately 48^o for the $N_\theta/N_\varphi = 0.15$ shape as r_b'/r_b varied from 1.00 to 0.80. The models were tested first with a square corner at the base $(r_c/r_b = 0)$ and then with a corner radius equal to 5 percent of the original base radius $(r_c/r_b = 0.05)$. The rounded corner decreased δ by an amount equivalent to a 5-percent reduction in the original base radius.

Maximum base radius for the models was 0.625 inch (1.59 cm). Coordinates for the unmodified tension shell shapes with zero corner radius are given in table I. All

models were machined from 17-4 PH stainless steel and were polished to a finish of approximately 10 microinches (250 nm).

Apparatus

Test facility.- The present investigation was conducted in the 9- by 6-inch model tunnel at the Langley Research Center (ref. 4). This facility is a supersonic blowdown wind tunnel which operates at a Mach number of 3.0 at stagnation pressures from 50 to 200 pounds per square inch absolute (345 to 1380 kN/m^2) and at stagnation temperatures from ambient to 3000° F (300° K to 1920° K). The air storage and pumping capacity are sufficient to permit continuous operation of the model tunnel at ambient stagnation temperature. Calibration tests of the tunnel test section showed a maximum deviation in Mach number of less than 1 percent.

The models were sting mounted to a mechanism capable of pitching the model through 12° angle of attack. Angle of attack was indicated on an ammeter which recorded the output from a linear potentiometer attached to the angle-of-attack mechanism. The angle-of-attack readings do not take into account sting deflection due to model air loads, but static load calculations show that the sting deflection should not exceed 0.3°.

Instrumentation.- Aerodynamic forces and pitching moments were measured with a three-component, strain-gage balance which was externally mounted with respect to the model. An aerodynamic shroud was used to shield the sting-balance assembly from the airstream, and a light was installed to indicate contact between shroud and sting.

Model base pressure was measured by means of an orifice tube located near the base of the model, and a chromel-alumel thermocouple attached to the model base indicated average model temperature. The pressure probe and thermocouple were located 180° apart in the yaw plane. Care was exercised in the thermocouple installation to preclude any interference with aerodynamic force measurements. Outputs from the pressure transducers, thermocouples, and strain-gage balance were recorded by the Langley central data recording system.

A single-pass horizontal Z-light-path schlieren system with a horizontal knife edge was used to observe the flow pattern along the models. A 70-mm camera, synchronized with a flashing light source, was used to photograph the shock patterns at a rate of 10 frames per second and at exposure times of a few microseconds.

The estimated accuracy of the measured data is as follows:

C_A	±0.020
C_D	±0.020
C_m	±0.010
C_N	±0.010

Tests

All tests were conducted at ambient stagnation temperature and at stagnation pressure levels of 60 and 170 pounds per square inch absolute (414 and 1170 kN/m^2). Corresponding Reynolds numbers, based on original model base diameter, were approximately 1.0×10^6 and 3.0×10^6, and the ratio of model temperature to stagnation temperature was approximately 0.97. All models were tested at angles of attack from 0^o to 12^o in 3^o increments.

The test procedure was to start the tunnel with a model set at an angle of attack of 0^o and maintain a stagnation pressure of 60 pounds per square inch absolute (414 kN/m^2) until the model temperature reached equilibrium. Data were then recorded at 60 and 170 pounds per square inch absolute (414 and 1170 kN/m^2) at each angle of attack during a single tunnel run. No data were acquired during the change from one angle of attack to another. Each stagnation pressure level was maintained for approximately 5 seconds to ensure an equilibrium base-pressure response.

All experimental drag and axial-force data presented herein are corrected to a free-stream static-pressure condition at the model base. Actual measured C_D and C_A values were approximately 0.11 higher than those shown. The moment center was $0.5r_b$ upstream from the original model base (fig. 1).

RESULTS AND DISCUSSION

In the investigation of reference 1, the pointed model (unmodified) encountered leeward flow separation from the tip at angles of attack of 9^o and above, whereas both blunted models encountered extensive flow separation at $\alpha = 0^o$. A summary of the boundary-layer separation events encountered by the models for all base modifications at all values of α and R for this investigation is presented in table II. A vertical line within a square is symbolic of the standing wave which is part of the double shock-wave pattern generated by these shapes as shown in figure 3. The shaded areas denote the extent of flow separation. (See sketch with table II.) Intersecting diagonals within a square represent a condition of uncertainty as to whether the boundary layer is, in fact, attached or separated. The uncertainty arises from difficulty in interpreting some schlieren photographs which show a series of shock-wave—boundary-layer interactions behind the standing wave. The results indicate beneficial effects relative to flow separation due to both base-radius reduction and rounding the corner at the base on all models except the $N_\theta/N_\varphi = 0.15$ model, for which the flow remained separated at $\alpha = 0^o$ even for a base radius of $0.75r_b$. Consequently, the detailed test results for this configuration are not presented.

Pointed Model

Flow pattern.- The most noticeable effect of base radius (and, hence, flow turning angle) is a downstream movement of the separation point for a given angle of attack (table II). This effect becomes more immediately evident from the schlieren photographs of figure 4. In this figure, the pointed model with zero corner radius at the base $\left(r_c/r_b = 0\right)$ and with the base corner rounded $\left(r_c/r_b = 0.05\right)$ is shown oriented at $\alpha = 12^o$ and $R \approx 3.0 \times 10^6$. With maximum base radius leeward flow separation occurs from the tip, but each reduction in base radius moves the leeward separation point farther downstream. The separation point for the models with the rounded corner is farther downstream at a given base radius than that for the models with zero corner radius. This effect is the result of an additional decrease in the flow turning angle δ due to the corner radius.

The data of table II show that, at the low Reynolds number, an attached boundary layer was maintained along the leeward surface as far downstream as the standing wave through $\alpha = 12^o$ for $r_b'/r_b = 1.00$ when the corner was rounded ($\delta = 82^o$). Attached flow up to the standing wave through $\alpha = 12^o$ was obtained at the high Reynolds number for $r_b'/r_b \leqq 0.85$ ($\delta \leqq 68^o$) as shown in figure 4. Although a distinctly separated boundary layer cannot be seen behind the standing wave at these values of r_b'/r_b, disturbances to the boundary layer are present and are indicated in table II by the intersecting diagonals. Complete flow attachment through $\alpha = 12^o$ without any boundary-layer disturbances was obtained only for $r_b'/r_b = 0.80$ with $r_c/r_b = 0.05$ ($\delta = 56^o$) at both Reynolds numbers.

The effect of Reynolds number, as shown in table II, appears contrary to expectations in that flow separation is more extensive at the high Reynolds number for both corner radii ($\delta < 90^o$). Other investigators (ref. 5, for example) have observed an increase in flow-field fluctuations as Reynolds number increased on spherically blunted tension shell shapes, but the extent of flow separation appeared generally unaffected.

Aerodynamic characteristics.- Typical effects of base radius on drag for the pointed model at $\alpha = 0^o$ are shown in figure 5. The drag coefficient C_D is plotted against the base radius ratio r_b'/r_b for corner-radius—base-radius ratios r_c/r_b of 0 and 0.05. Drag coefficients are also shown for a disk and 45^o and 60^o semivertex angle cones from reference 1. The data indicate a decline in C_D with base radius for both sharp and round corners, as would be expected. Higher C_D values are obtained, however, for models with zero corner radius, not only at the same value of r_b'/r_b but also at the same value of flow turning angle δ, as shown in figure 6. Attached flow up to the standing wave through $\alpha = 12^o$ was accompanied by a 7-percent average loss in C_D with respect to the unmodified body with zero corner radius. For this condition, the C_D value is approximately 11 percent higher than that of the 60^o semivertex angle

cone. The configuration required for complete flow attachment through $\alpha = 12^{\circ}$ without the presence of boundary-layer disturbances behind the standing wave has a C_D value approximately 5 percent below that of the 60° semivertex angle cone at $R \approx 3.0 \times 10^6$. This value represents a loss in C_D of approximately 19 percent with respect to the unmodified body with zero corner radius.

The effects of base radius on pitching-moment, axial-force, and normal-force coefficients are shown in figure 7 for the pointed model with both corner radii. The dashed lines denote the angle-of-attack interval within which leeward flow separation was known to have occurred. As in reference 1, the results indicate an abrupt change in the aerodynamic coefficients when flow separation occurs. This effect is most severe when the separation point is farthest upstream and diminishes with r_b'. As the base radius was reduced, the slope of the C_m curve at $\alpha = 0^{\circ}$ generally decreased while the slope of the C_N curve at $\alpha = 0^{\circ}$ increased as shown in figure 8. Such variations are indicative of greater static stability. Reducing the base radius also resulted in a movement of the center of pressure from positions upstream of the nose to positions downstream of the moment center for both corner radii, as shown in figure 9. The centers of pressure shown for the blunt models are discussed subsequently.

Spherically Blunted Model

Flow pattern.- For the spherically blunted model, an attached boundary layer was obtained at $\alpha = 0^{\circ}$ for $r_b'/r_b = 0.90$ ($\delta = 74.7^{\circ}$) although disturbances to the flow occurred downstream of the standing wave as shown in figure 10. Attached flow without disturbances at $\alpha = 0^{\circ}$ was achieved for $r_b'/r_b = 0.80$ ($\delta \leq 62^{\circ}$), but for the present modifications an attached boundary layer could not be maintained downstream of the standing wave on the leeward surface at $\alpha > 3^{\circ}$ (table II). Hence, with respect to the pointed model, a smaller base radius (or flow turning angle) is required of the spherically blunted model to attain a given location of the separation point at a given angle of attack. This effect is observed from the flow patterns of figures 11 and 4. The effect of Reynolds number, unlike that for the pointed model, was as expected in that the separation point moved downstream when the Reynolds number was increased. (See table II.)

Aerodynamic characteristics.- The effects of base radius and corner radius on C_D at $\alpha = 0^{\circ}$ are shown in figures 12 and 13 for the spherically blunted model. Unlike the data for the pointed model (fig. 5), C_D shows an increase for the first few reductions in base radius. This effect was the result of the movement of the separation point to positions downstream of the nose. Once the separation point reached the standing wave, however, the effect of further reduction in base radius was similar to that for the pointed model – that is, C_D decreased. In general, the C_D values of the spherically

blunted models with an attached boundary layer up to the standing wave were a little less than those of the pointed model.

The effects of base radius and corner radius on the aerodynamic coefficients are shown in figure 14. When the boundary layer separates at $\alpha = 0^{\circ}$, an increase in α results in a downstream movement of the windward separation point and an upstream movement of the leeward separation point. Consequently, as shown in figures 14(a) to (c) for $r_b'/r_b = 1.00$, C_A increases until the windward boundary layer becomes attached. Similar large changes occur in the variation of C_m and C_N. When the reduction in the base radius was sufficient to cause the movement of the separation point downstream from the nose at $\alpha = 0^{\circ}$, C_m, C_A, and C_N varied smoothly with α. The large values of C_m and C_N shown at $\alpha = 0^{\circ}$ in figure 14 for $r_b'/r_b = 1.00$ and 0.95 are attributable to a slightly negative α as evidenced by schlieren photographs which show an asymmetric flow pattern around these shapes which, in turn, indicates a strong sensitivity to α.

Centers of pressure were evaluated from C_m and C_N data only for those shapes which showed attached flow at least to the standing wave through $\alpha = 3^{\circ}$. For the spherically blunted models, this condition was met only for $r_b'/r_b = 0.80$ ($\delta = 62^{\circ}$) with zero corner radius at the low Reynolds number and for $r_b'/r_b = 0.85$ ($\delta = 62^{\circ}$) with the round corner at both Reynolds numbers. These points are shown in figure 9 by the solid symbols. For these models, the centers of pressure were downstream from the moment center. A comparison of the pointed and spherically blunted model data (fig. 8) shows better static stability for the spherically blunted model.

CONCLUSIONS

An investigation was undertaken to explore the effectiveness of tension-shell configuration modifications intended to delay boundary-layer flow separation and, hence, to minimize degradation of static aerodynamic characteristics. The modifications decreased the angle through which the flow along the body is turned (from 90° to approximately 56°) and consisted of reducing the base radius in 5-percent increments to 80 percent of the original radius while maintaining a corner radius of either 0 or 5 percent of the original base radius. Three configurations were tested. One configuration was pointed and encountered leeward flow separation at an angle of attack of 9° before modification. The other two configurations were spherically blunted (one was a spherically blunted version of the pointed configuration) and encountered extensive flow separation at 0° angle of attack before modification. Static aerodynamic characteristics were obtained from tests conducted at a Mach number of 3.0, at angles of attack up to 12°,

and at Reynolds numbers, based on original base diameter, of approximately 1.0×10^6 and 3.0×10^6. The test results indicated the following conclusions:

1. For the pointed model and its spherically blunted version, reducing the base radius and rounding the corner at the base delayed flow separation and improved static stability. For the other spherically blunted model, attached flow could not be achieved at an angle of attack of 0° for the modifications tested.

2. For the pointed model, the modifications were effective in maintaining attached flow through an angle of attack of 12° and caused a shift in the center of pressure from positions upstream of the nose to positions downstream of the moment center. The modifications, however, also resulted in a decrease in drag coefficient at an angle of attack of 0°.

3. For the spherically blunted version of the pointed model, attached flow was achieved at an angle of attack of 0° when the modifications yielded a flow turning angle of approximately 75° (base radius reduced to 90 percent of original radius with zero corner radius), and the drag coefficient increased. When the flow turning angle was decreased further, the drag coefficient decreased at values a little less than those of the pointed model.

4. Attached flow could not be maintained on the leeward surface at angles of attack greater than 3° with the spherically blunted version of the pointed model for the modifications tested.

5. Where both the pointed model and its spherically blunted version showed attached flow through an angle of attack of 3°, better static stability was indicated for the spherically blunted model.

Langley Research Center,
National Aeronautics and Space Administration,
Langley Station, Hampton, Va., March 3, 1967,
124-08-06-03-23.

APPENDIX A

CONVERSION OF U.S. CUSTOMARY UNITS TO SI UNITS

The International System of Units (SI) was adopted by the Eleventh General Conference on Weights and Measures held in Paris, October 1960, in Resolution No. 12 (ref. 2). Conversion factors required for units used herein are given in the following table:

Physical quantity	U.S. Customary Unit	Conversion factor (*)	SI Unit
Length	in.	0.0254	meters (m)
Pressure	psi	6.895×10^3	newtons/meter^2 (N/m^2)
Temperature	(^{o}F + 460)	5/9	degrees Kelvin (^{o}K)

*Multiply value given in U.S. Customary Unit by conversion factor to obtain equivalent value in SI Unit.

Prefixes to indicate multiples of units are as follows:

Prefix	Multiple
nano (n)	10^{-9}
centi (c)	10^{-2}
giga (G)	10^{9}
hecto (h)	10^{2}
kilo (k)	10^{3}
mega (M)	10^{6}

REFERENCES

1. Deveikis, William D.; and Sawyer, James Wayne: Aerodynamic Characteristics of Tension Shell Shapes at Mach 3.0. NASA TN D-3633, 1966.

2. Mechtly, E. A.: The International System of Units – Physical Constants and Conversion Factors. NASA SP-7012, 1964.

3. Anderson, Melvin S.; Robinson, James C.; Bush, Harold G.; and Fralich, Robert W.: A Tension Shell Structure for Application to Entry Vehicles. NASA TN D-2675, 1965.

4. Schaefer, William T., Jr.: Characteristics of Major Active Wind Tunnels at the Langley Research Center. NASA TM X-1130, 1965.

5. Jones, Robert A.; Bushnell, Dennis M.; and Hunt, James L.: Experimental Flow Field and Heat-Transfer Investigation of Several Tension Shell Configurations at a Mach Number of 8. NASA TN D-3800, 1967.

TABLE I.- COORDINATES OF TENSION SHELL SHAPES

r/r_b	x/r_b for –	
	$N_\theta/N_\varphi = 0$ $(\beta_o = 27.0^o,\ A^2 = 1.423)$	$N_\theta/N_\varphi = 0.15$ $(\beta = 23.5^o,\ A^2 = 0.900)$
0	1.192	(*)
.05	1.094	(*)
.10	.998	(*)
.15	.901	(*)
.20	.808	0.555
.25	.718	.481
.30	.630	.416
.35	.549	.357
.40	.469	.303
.45	.397	.255
.50	.330	.211
.55	.269	.171
.60	.214	.136
.65	.165	.104
.70	.122	.077
.75	.085	.054
.80	.054	.035
.85	.030	.020
.90	.014	.009
.95	.004	.002
1.00	0	0

*$r_n/r_b = 0.218$.

TABLE II. – SUMMARY OF BOUNDARY-LAYER SEPARATION EVENTS

$\frac{r_b'}{r_b}$	R	Surface	Occurrence of separated flow for —																													
			$N_\theta/N_\varphi = 0$																						$N_\theta/N_\varphi = 0.15$									
			$r_n/r_b = 0$									$r_n/r_b = 0.100$										$r_n/r_b = 0.218$										
			$r_c/r_b = 0$					$r_c/r_b = 0.05$				$r_c/r_b = 0$					$r_c/r_b = 0.05$					$r_c/r_b = 0$					$r_c/r_b = 0.05$				
			Angle of attack, deg																													
			0	3	6	9	12	0	3	6	9	12	0	3	6	9	12	0	3	6	9	12	0	3	6	9	12	0	3	6	9	12
1.00	1.0×10^6	Leeward						x																								
		Windward						x																								
	3.0×10^6	Leeward																														
		Windward																														
.95	1.0×10^6	Leeward																														
		Windward																														
	3.0×10^6	Leeward																														
		Windward																														
.90	1.0×10^6	Leeward																														
		Windward																														
	3.0×10^6	Leeward																														
		Windward																														
.85	1.0×10^6	Leeward																				x										
		Windward																				x										
	3.0×10^6	Leeward							x																							
		Windward							x																							
.80	1.0×10^6	Leeward	x																													
		Windward	x																													
	3.0×10^6	Leeward																														
		Windward																														
.75	1.0×10^6	Leeward	No test					No test					No test					No test										No test				
		Windward																														
	3.0×10^6	Leeward																														
		Windward																														

x No schlieren photograph

Separated flow uncertain

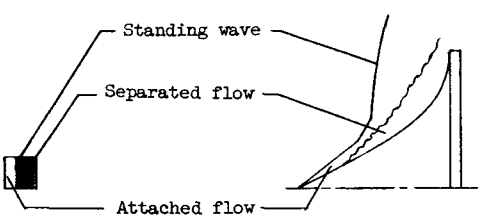

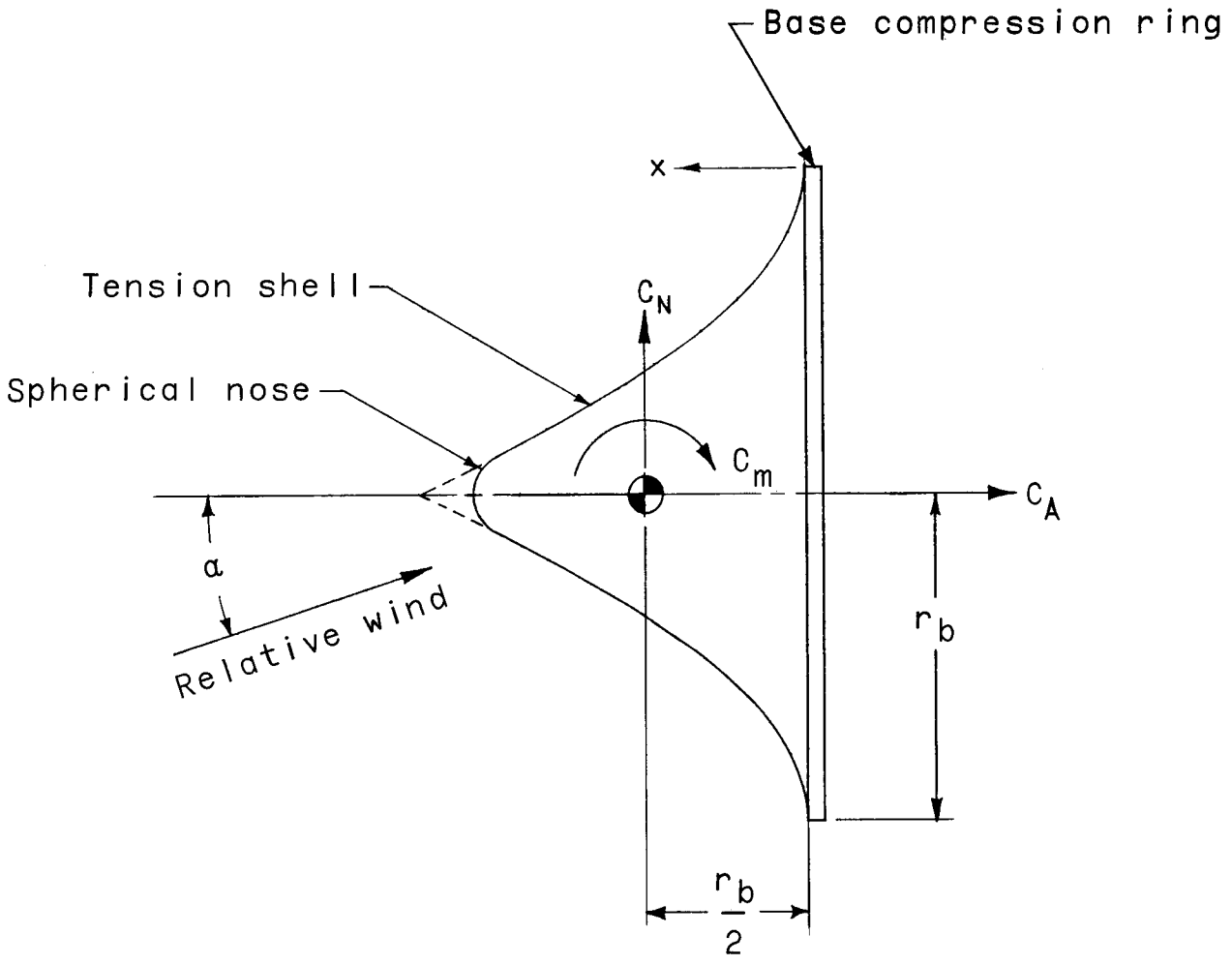

Figure 1.- Body axis system. Positive directions are indicated by arrows.

r_b'/r_b for –		δ, deg, for –	
$\frac{r_c}{r_b} = 0$	$\frac{r_c}{r_b} = .05$	$\frac{N_\theta}{N_\varphi} = 0$	$\frac{N_\theta}{N_\varphi} = .15$
1.00	———	90	90
.95	1.00	82	84
.90	.95	75	77
.85	.90	68	68
.80	.85	62	58
.75	.80	56	48

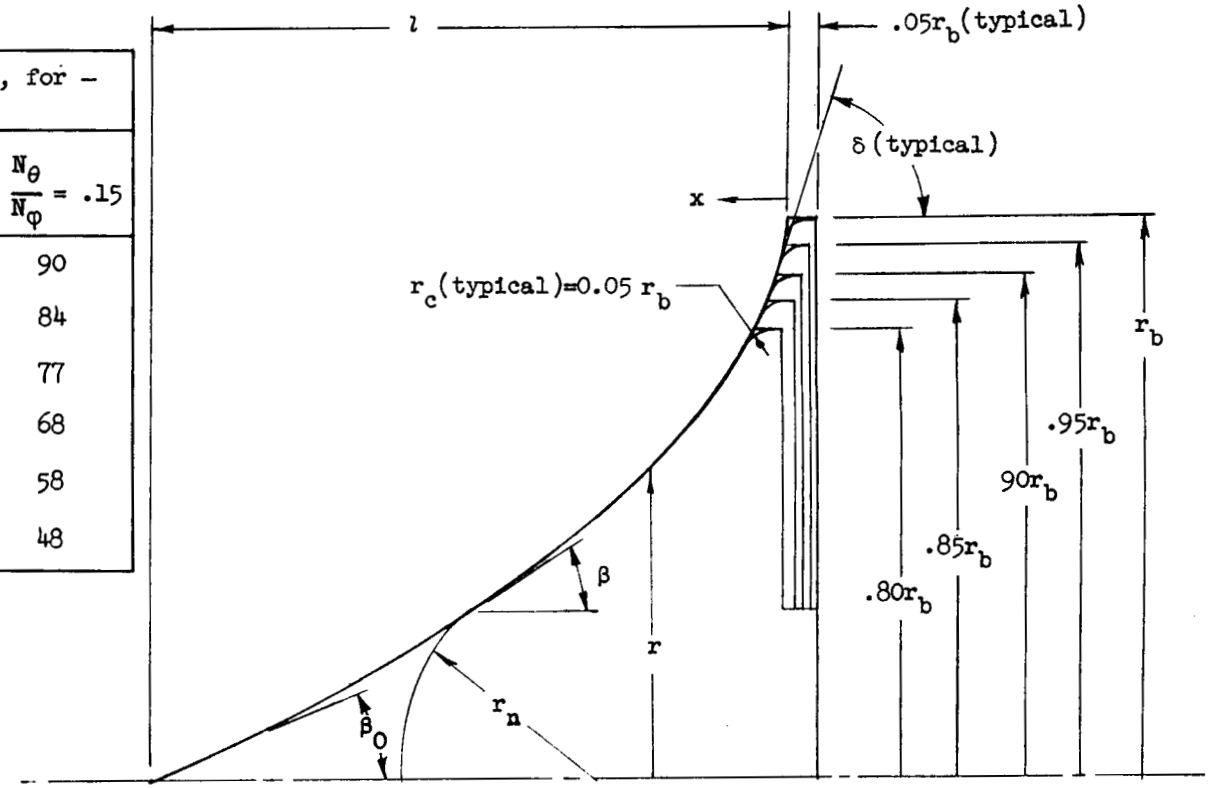

Figure 2.- Model details and base modifications. Maximum body radius r_b is 0.625 inch (1.59 cm).

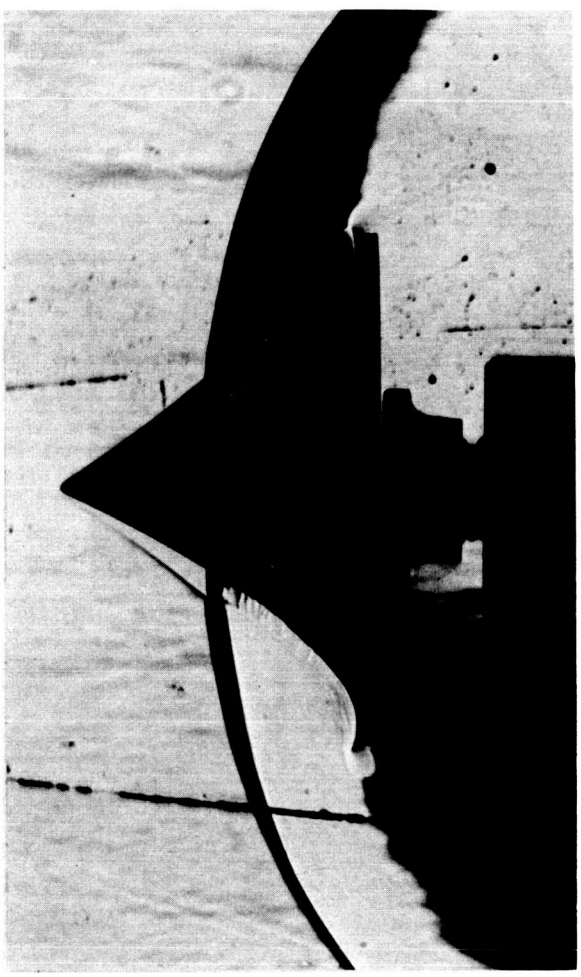

L-67-1013

Figure 3.- Model with double shock-wave pattern at 0^{o} angle of attack for $\frac{r_b'}{r_b} = 1.00$, $\frac{r_n}{r_b} = 0$, and $\frac{r_c}{r_b} = 0$ at $M = 3.0$ and $R \approx 3.0 \times 10^6$.

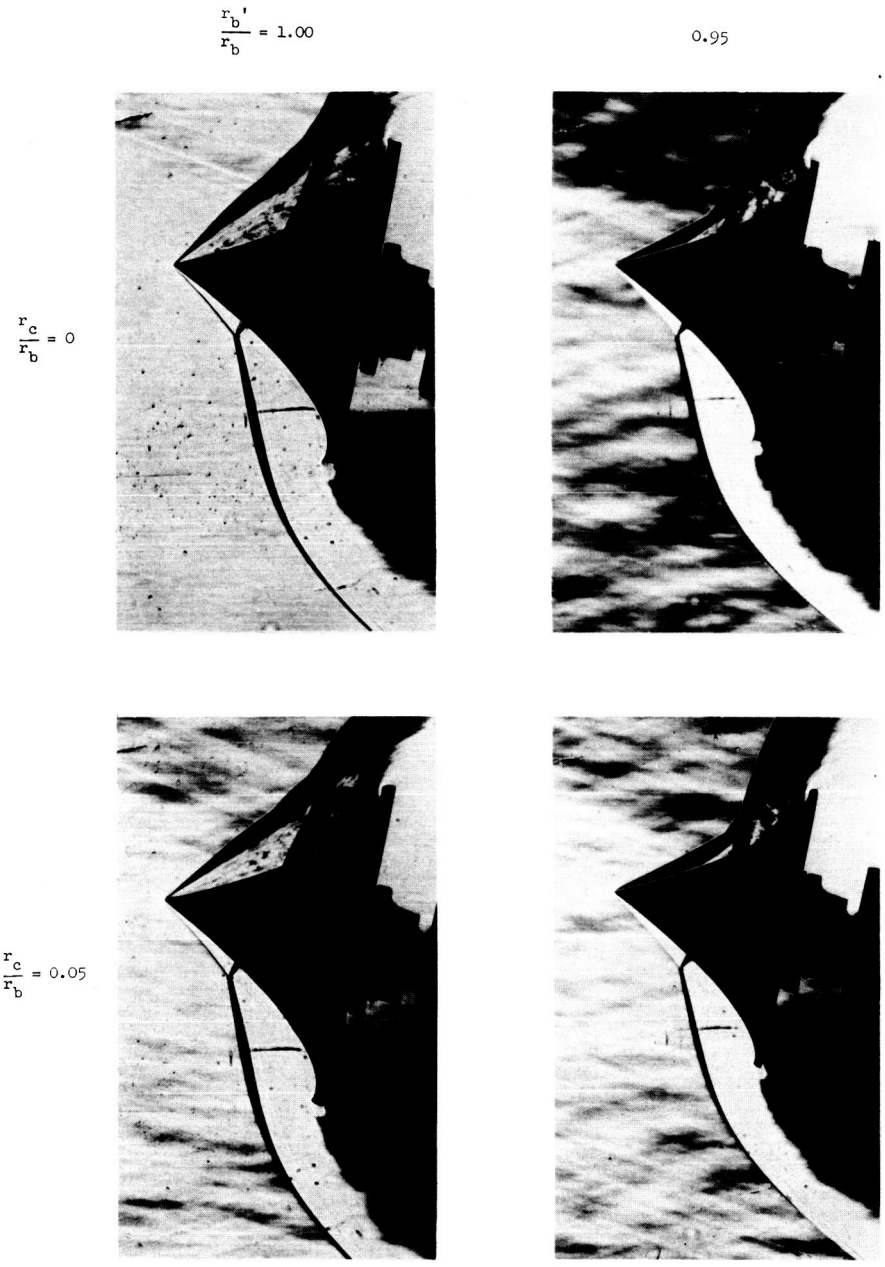

L-67-1014

Figure 4.- Effect of base radius on boundary-layer separation for $\frac{r_n}{r_b} = 0$ at $M = 3.0$, $R \approx 3.0 \times 10^6$, and $\alpha = 12^o$.

$\frac{r_b'}{r_b} = 0.90$ 0.85 0.80

$\frac{r_c}{r_b} = 0$

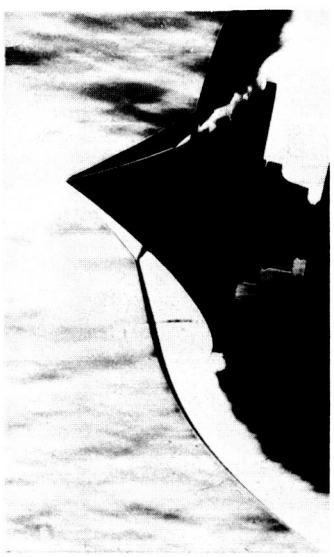
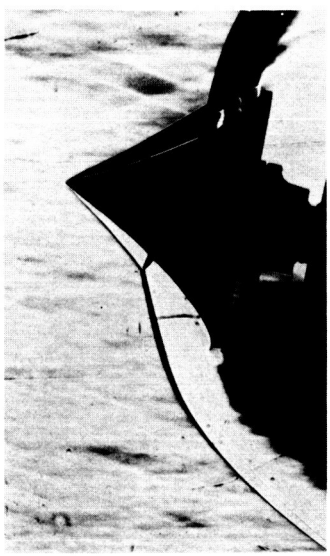
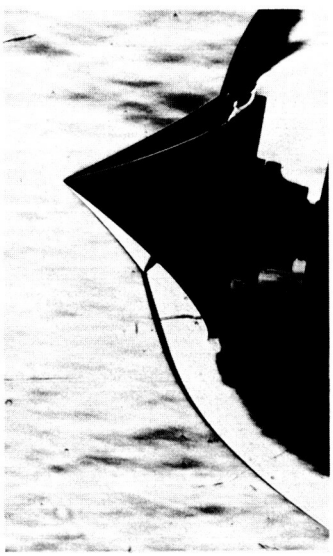

$\frac{r_c}{r_b} = 0.05$

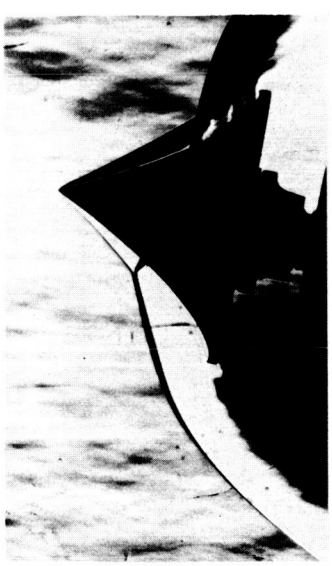
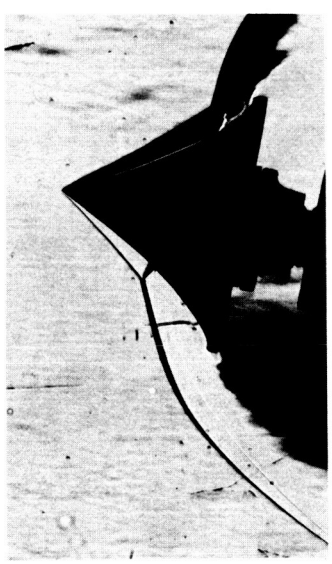
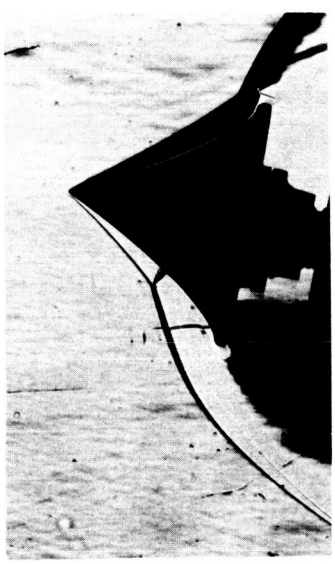

Figure 4.- Concluded.

L-67-1015

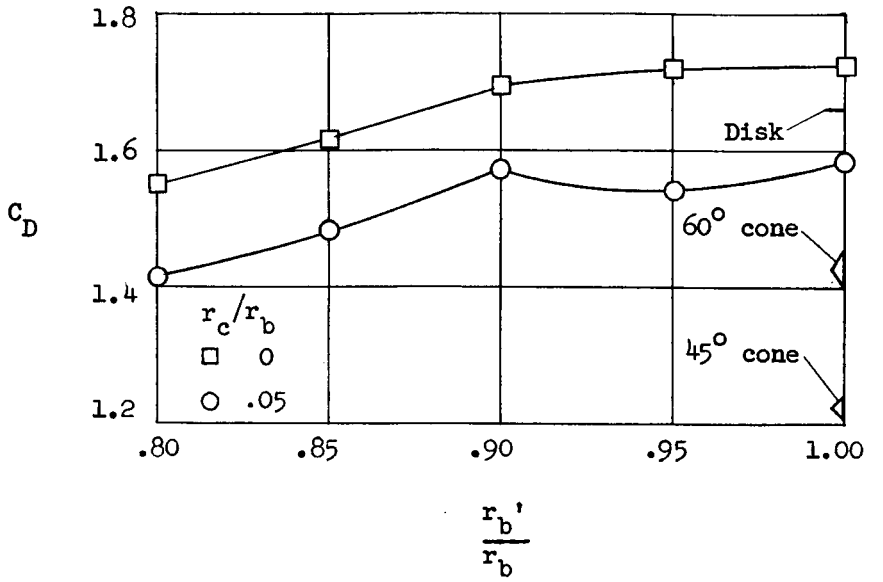

(a) $R \approx 1.0 \times 10^6$.

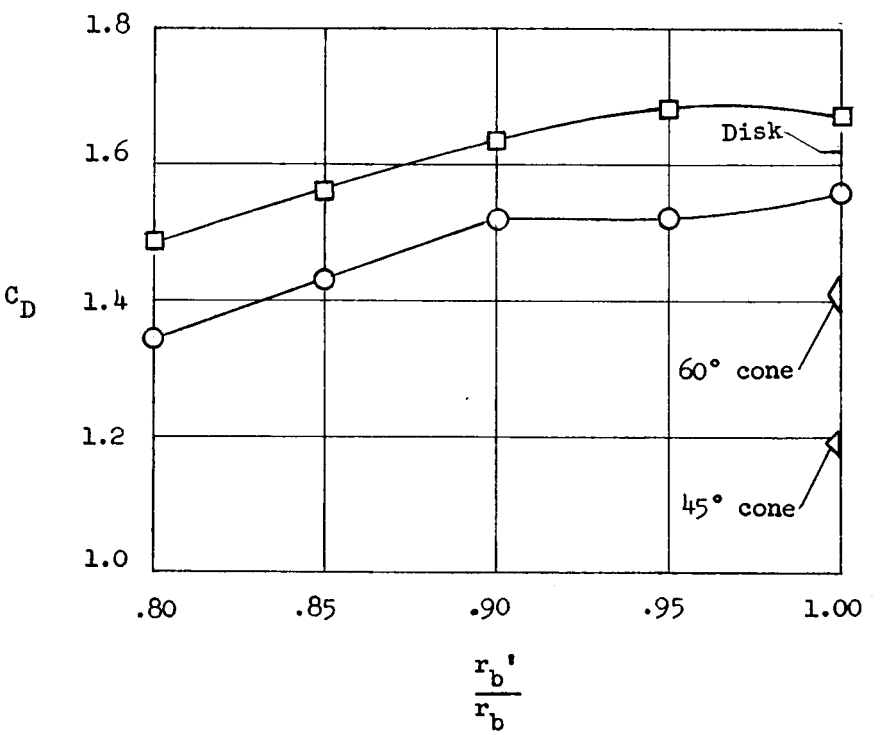

(b) $R \approx 3.0 \times 10^6$.

Figure 5.- Effect of base radius on drag coefficient at $\alpha = 0^o$ for $\frac{r_n}{r_b} = 0$ at $M = 3.0$.

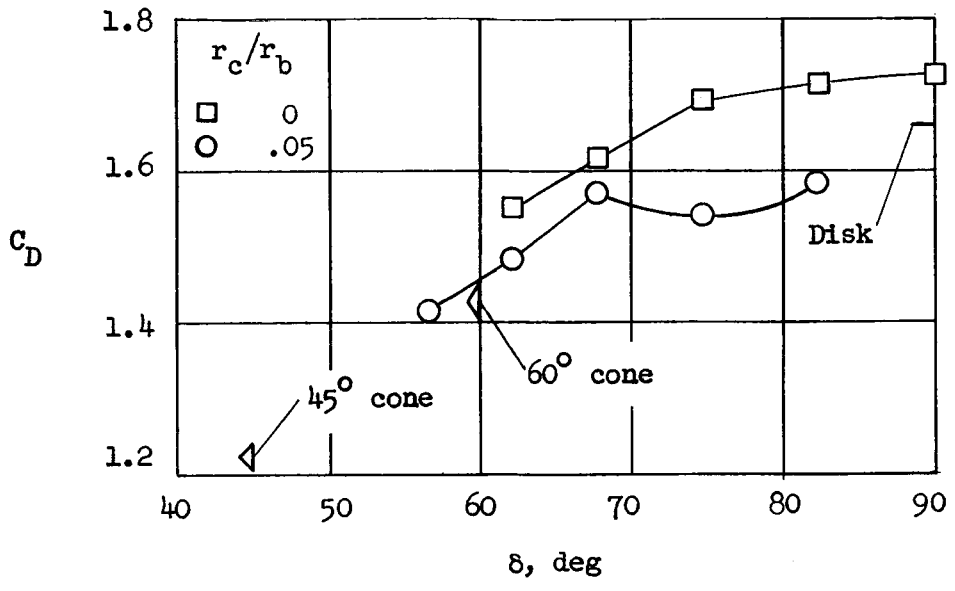

(a) $R \approx 1.0 \times 10^6$.

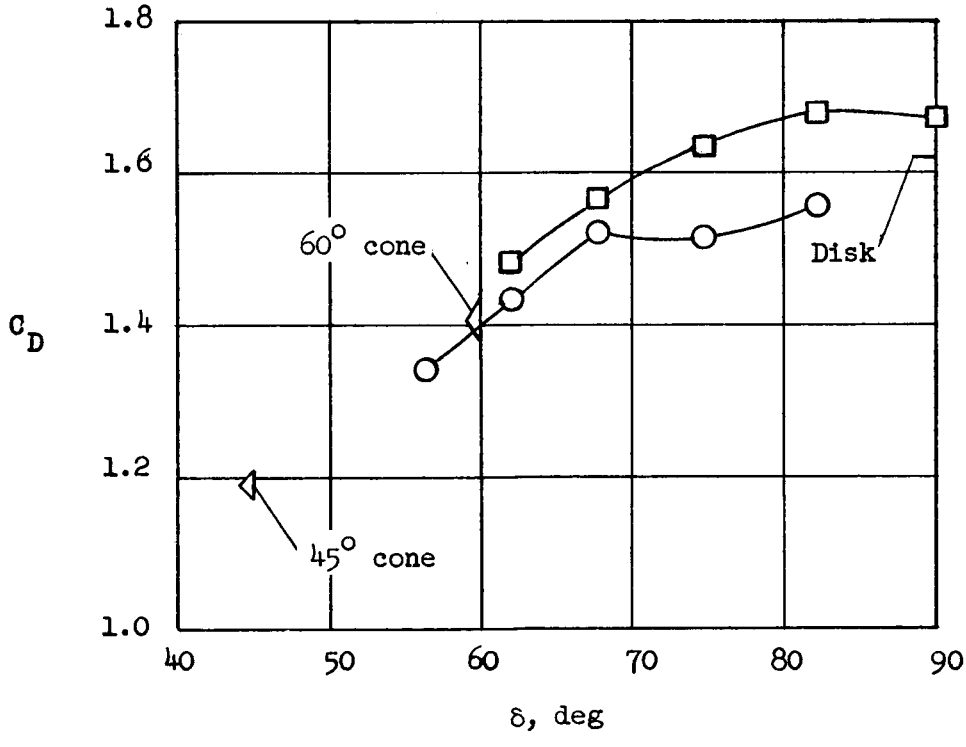

(b) $R \approx 3.0 \times 10^6$.

Figure 6.- Variation of drag coefficient at $\alpha = 0^0$ with flow turning angle for $\frac{r_n}{r_b} = 0$ at $M = 3.0$.

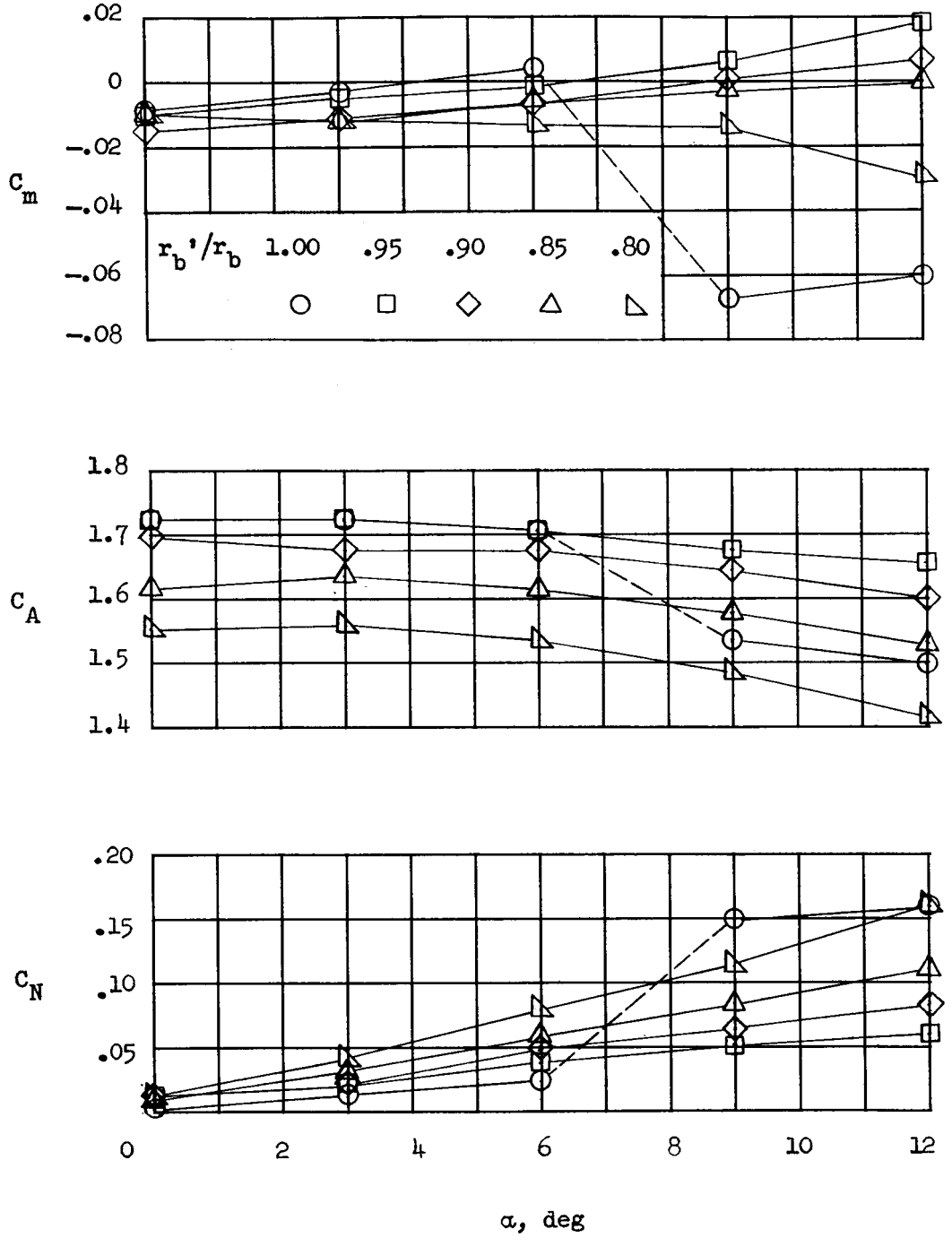

(a) $\frac{r_c}{r_b} = 0$; $R \approx 1.0 \times 10^6$.

Figure 7.- Effects of base radius on longitudinal aerodynamic characteristics for $\frac{r_n}{r_b} = 0$ at $M = 3.0$.

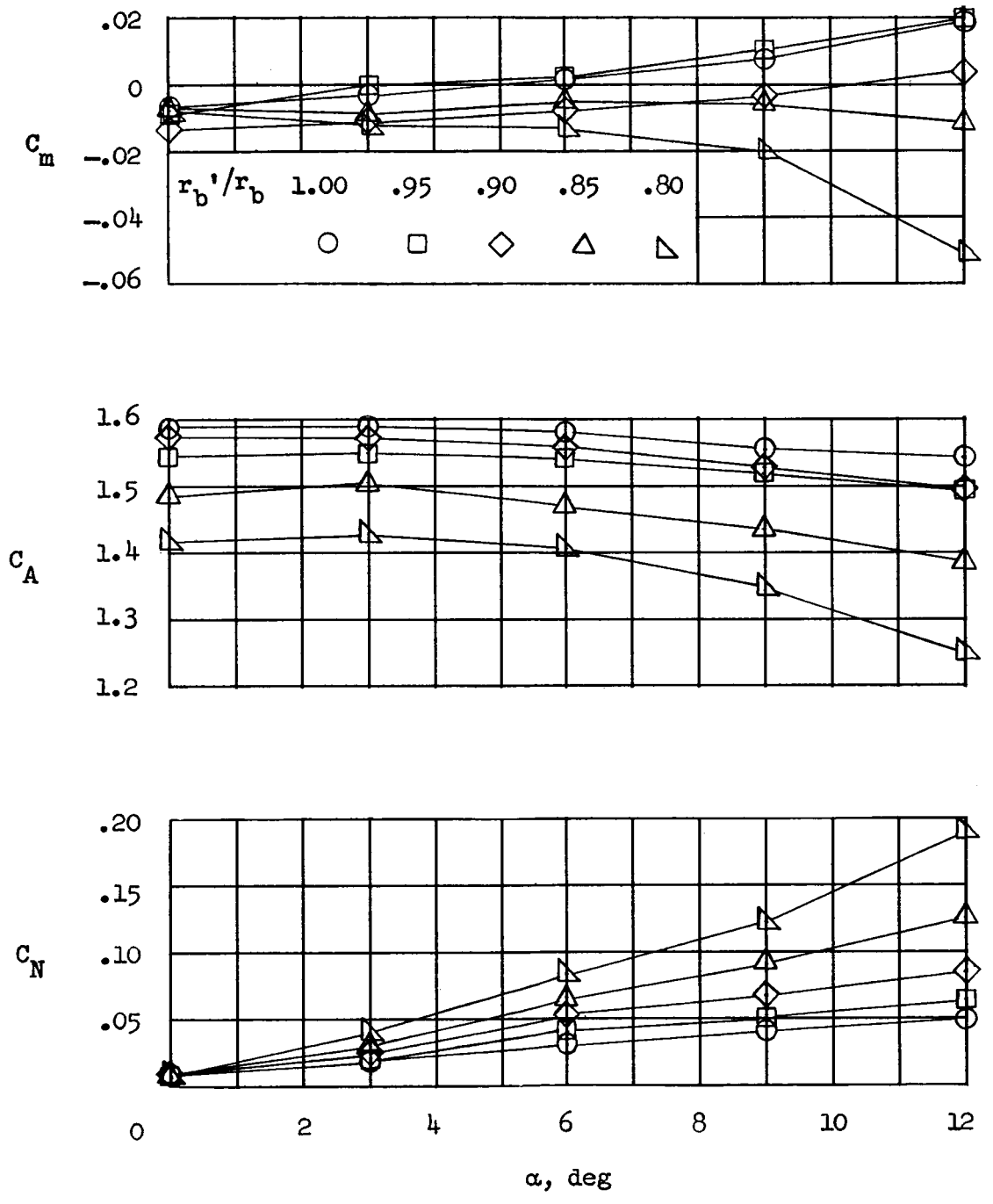

(b) $\frac{r_c}{r_b} = 0.05$; $R \approx 1.0 \times 10^6$.

Figure 7.- Continued.

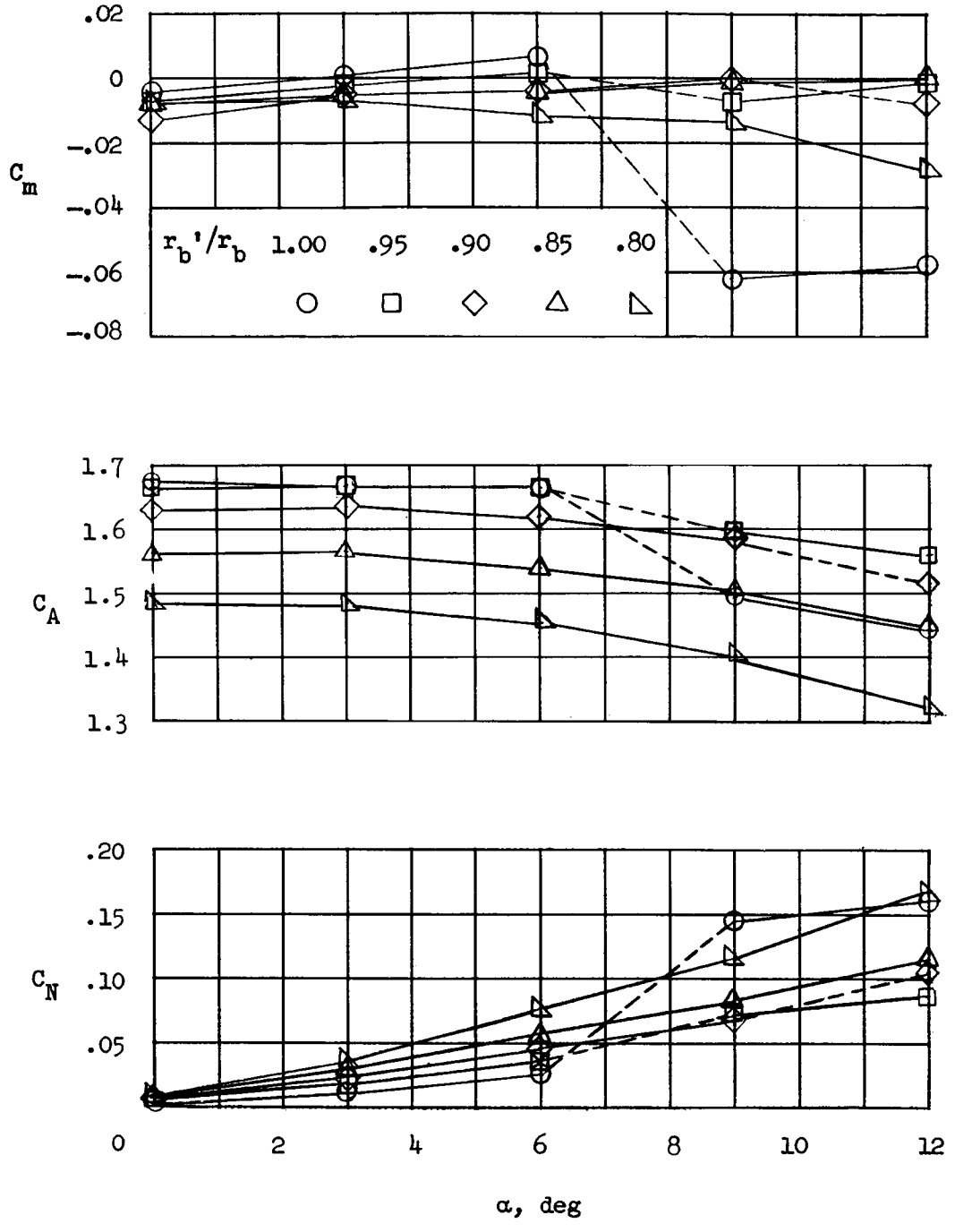

(c) $\frac{r_c}{r_b} = 0$; $R \approx 3.0 \times 10^6$.

Figure 7.- Continued.

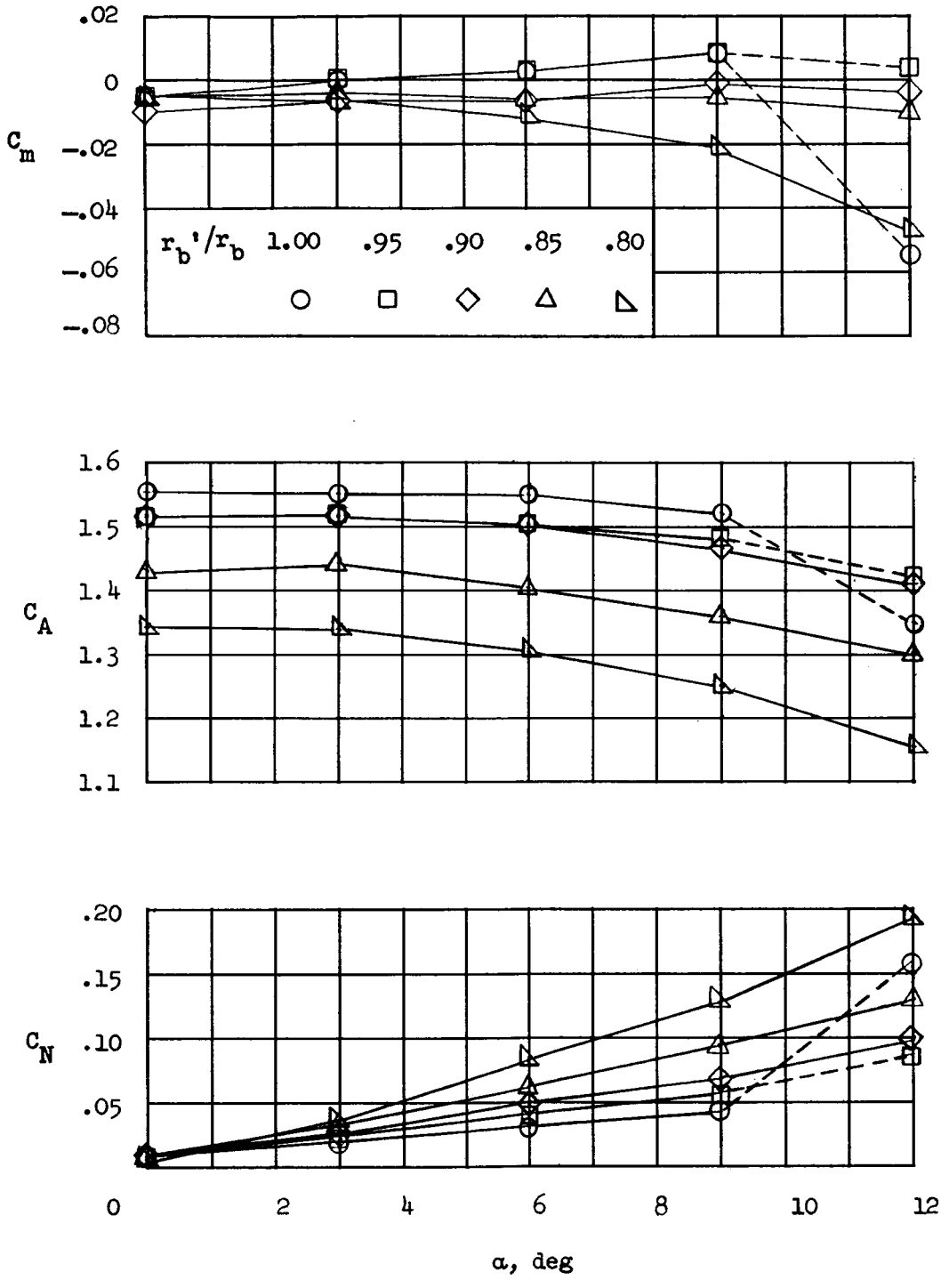

(d) $\frac{r_c}{r_b} = 0.05$; $R \approx 3.0 \times 10^6$.

Figure 7.- Concluded.

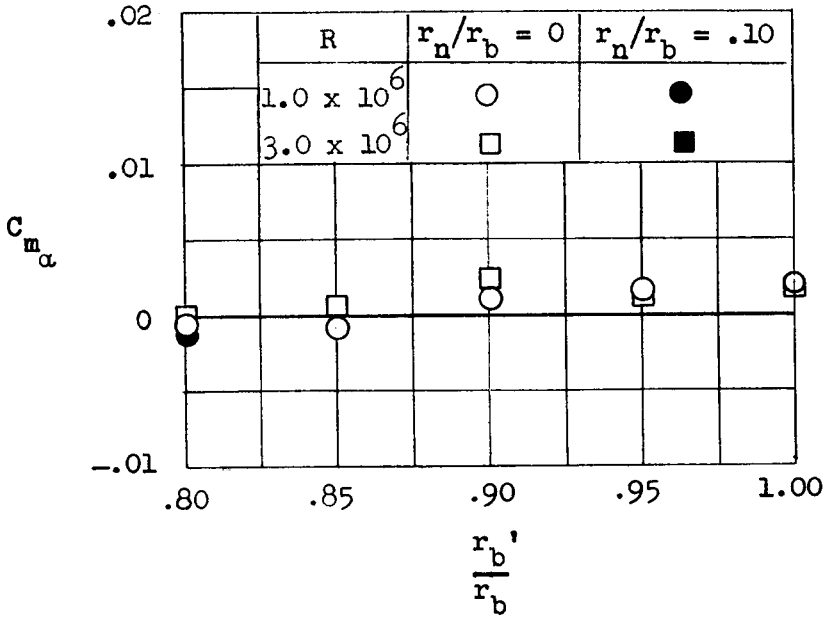

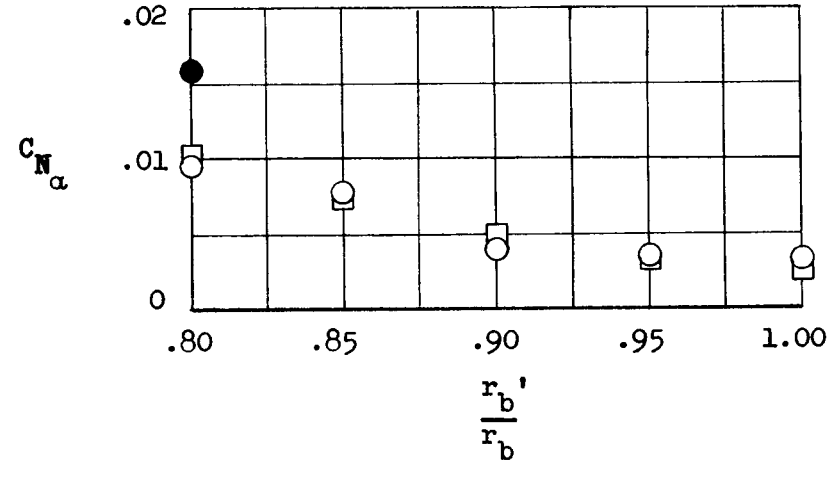

(a) $\frac{r_c}{r_b} = 0.$

Figure 8.- Variation of C_{m_α} and C_{N_α} with base radius at M = 3.0.

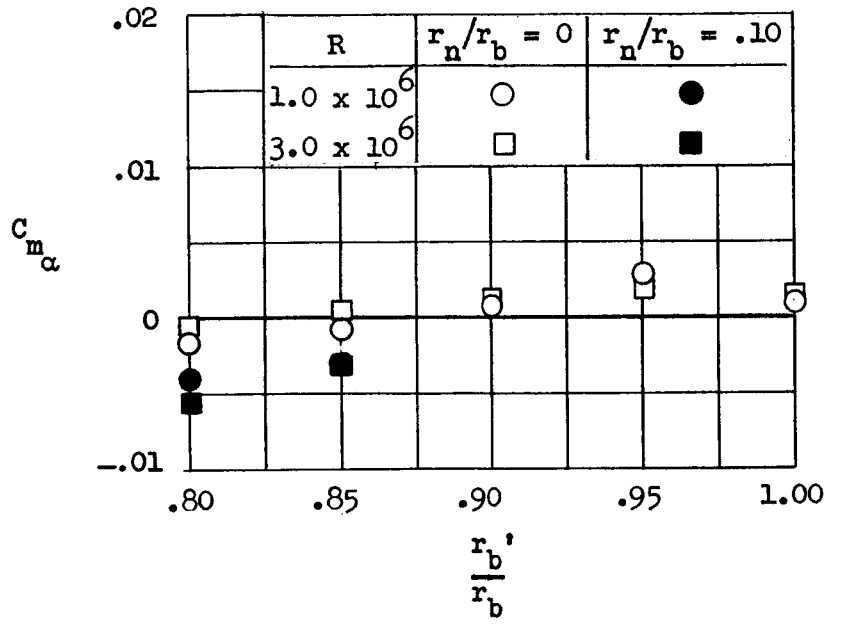

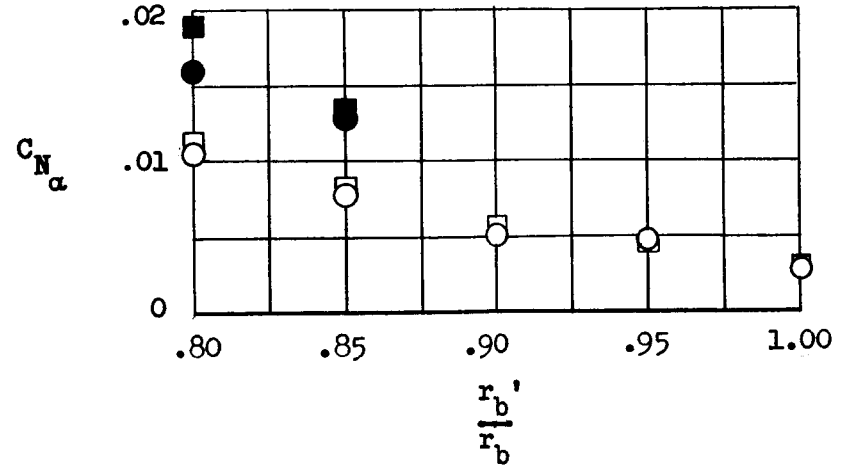

(b) $\frac{r_c}{r_b} = 0.05$.

Figure 8.- Concluded.

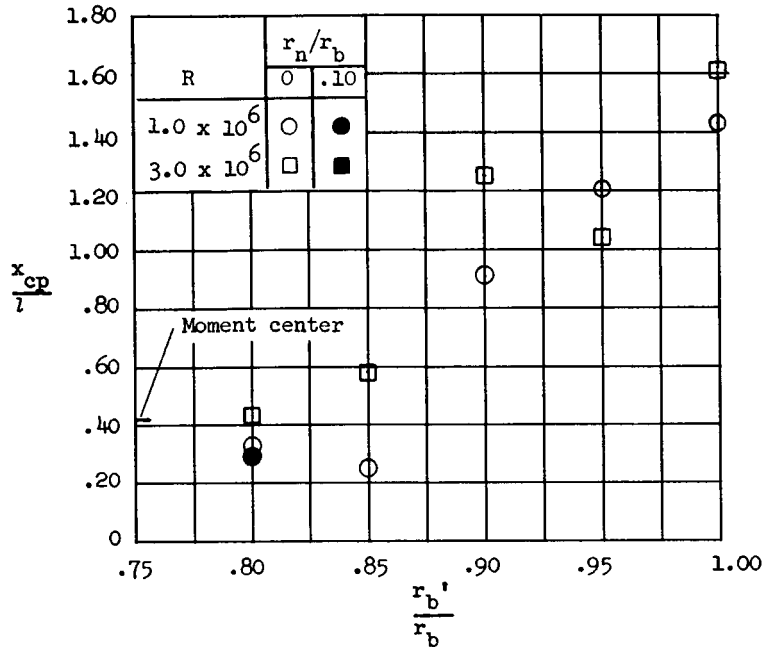

(a) $\frac{r_c}{r_b} = 0.$

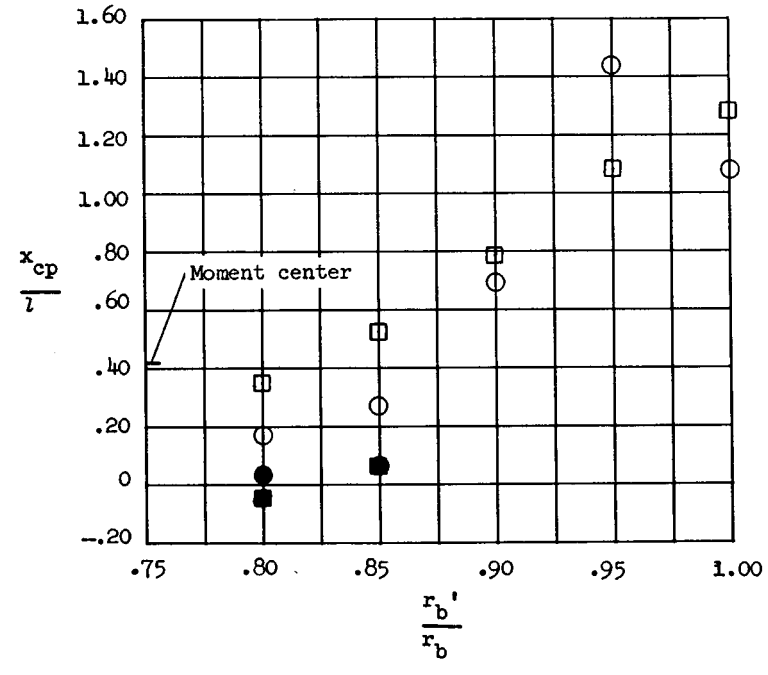

(b) $\frac{r_c}{r_b} = 0.05.$

Figure 9.- Effect of base radius on center of pressure.

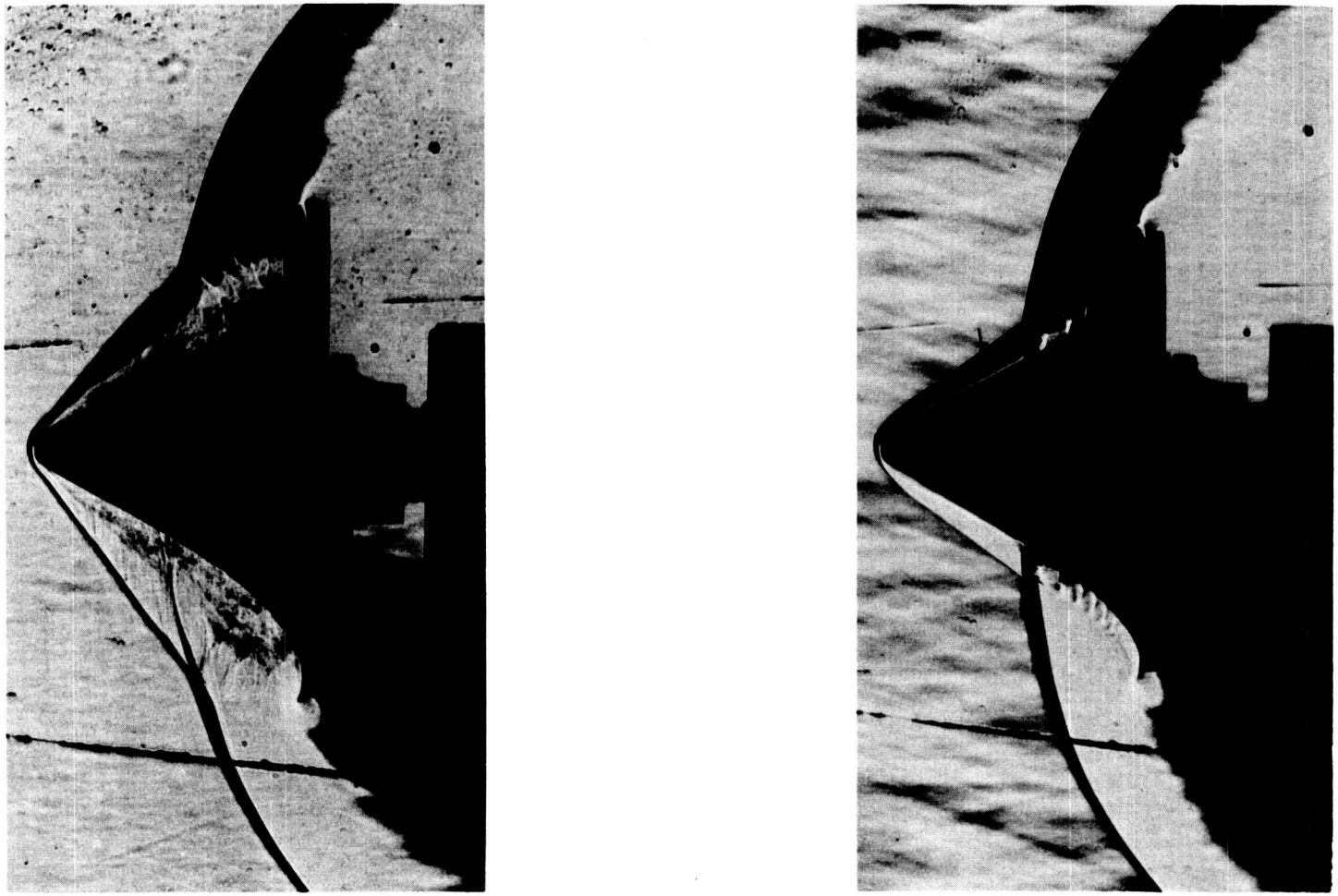

(a) $\frac{r_b'}{r_b} = 1.00.$

(b) $\frac{r_b'}{r_b} = 0.90.$

L-67-1016

Figure 10.- Effect of base radius on boundary-layer separation at $\alpha = 0^o$ for $\frac{r_n}{r_b} = 0.10$ and $\frac{r_c}{r_b} = 0$ at $M = 3.0$ and $R \approx 3.0 \times 10^6$.

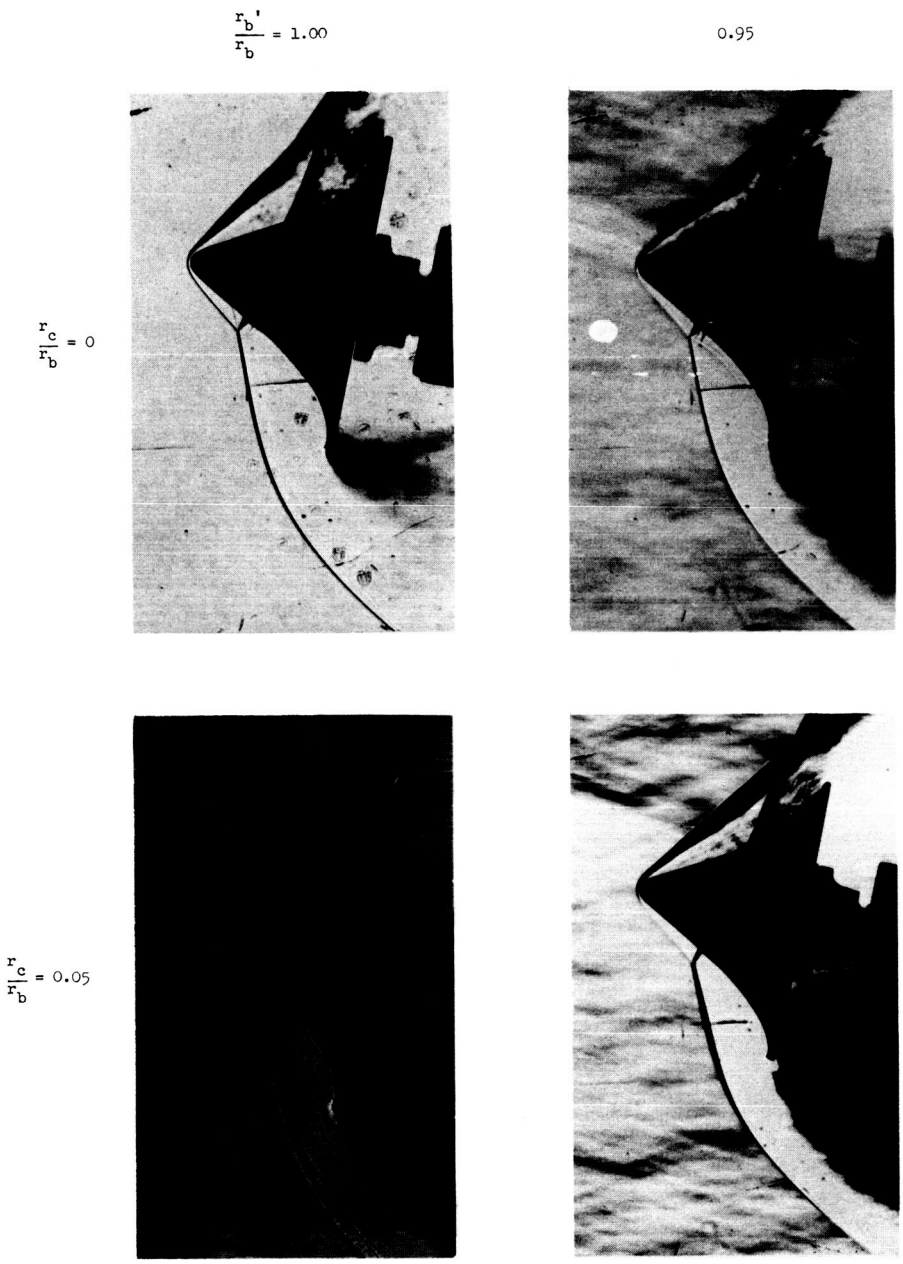

L-67-1017

Figure 11.- Effect of base radius on boundary-layer separation for $\frac{r_n}{r_b} = 0.10$ at $M = 3.0$, $R \approx 3.0 \times 10^6$, and $\alpha = 12^0$.

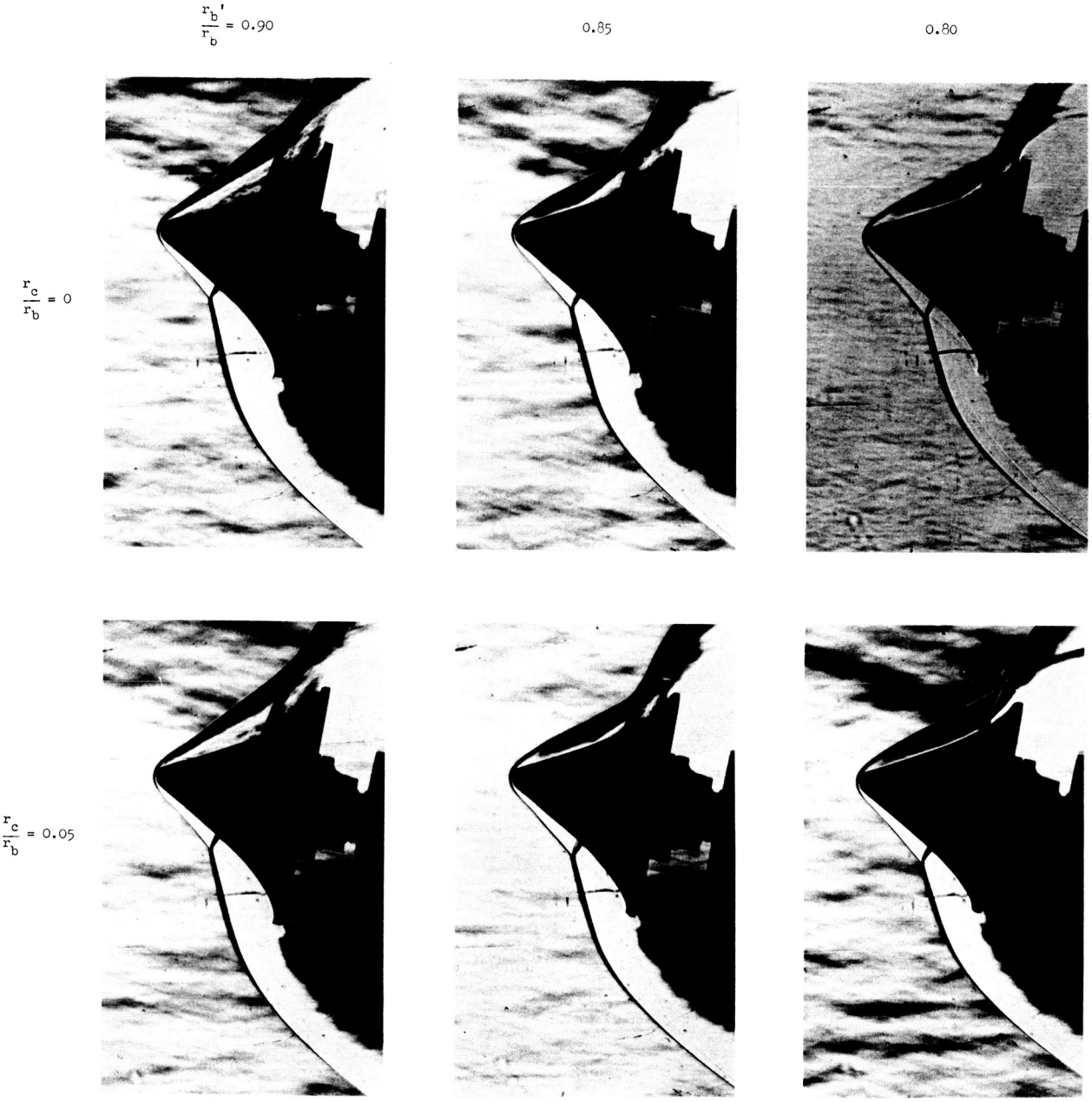

Figure 11.- Concluded.

L-67-1018

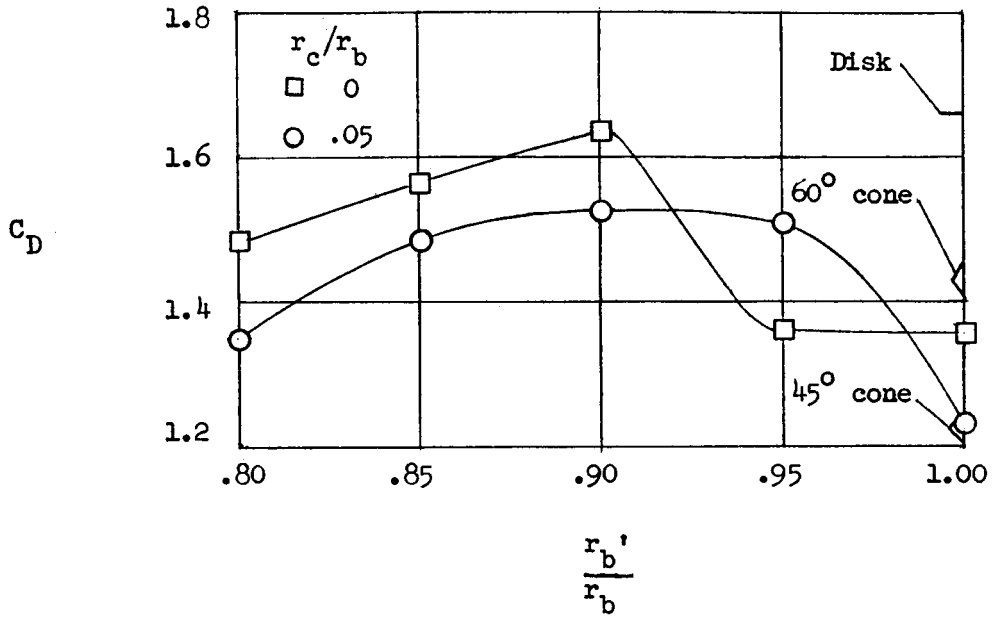

(a) $R \approx 1.0 \times 10^6$.

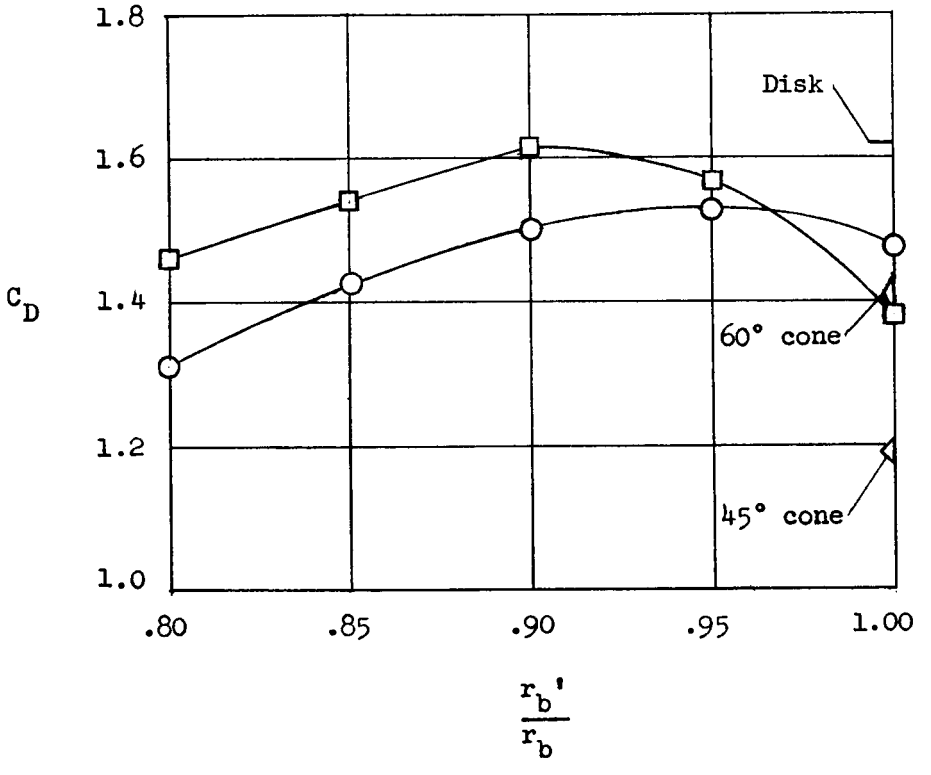

(b) $R \approx 3.0 \times 10^6$.

Figure 12.- Effect of base radius on drag coefficient at $\alpha = 0^0$ for $\frac{r_n}{r_b} = 0.10$ at $M = 3.0$.

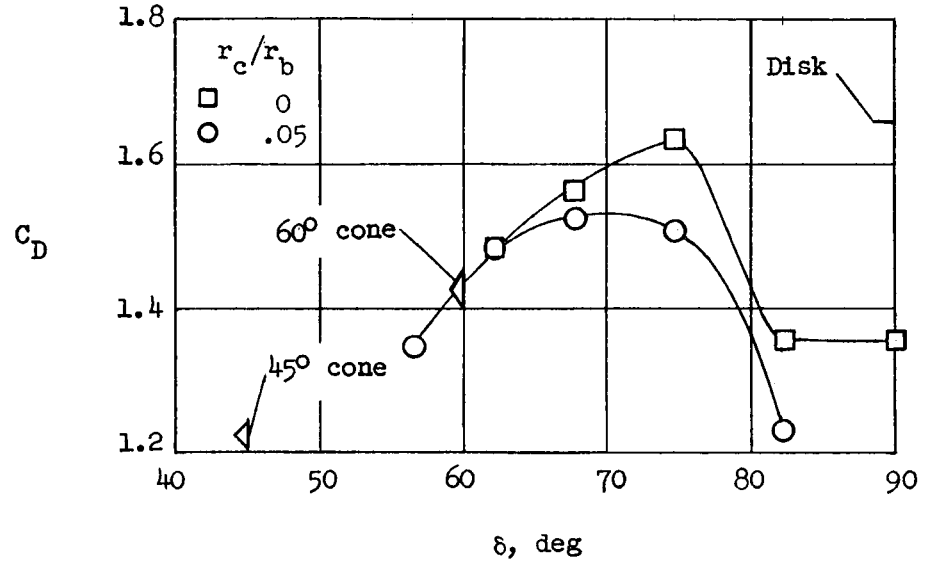

(a) $R \approx 1.0 \times 10^6$.

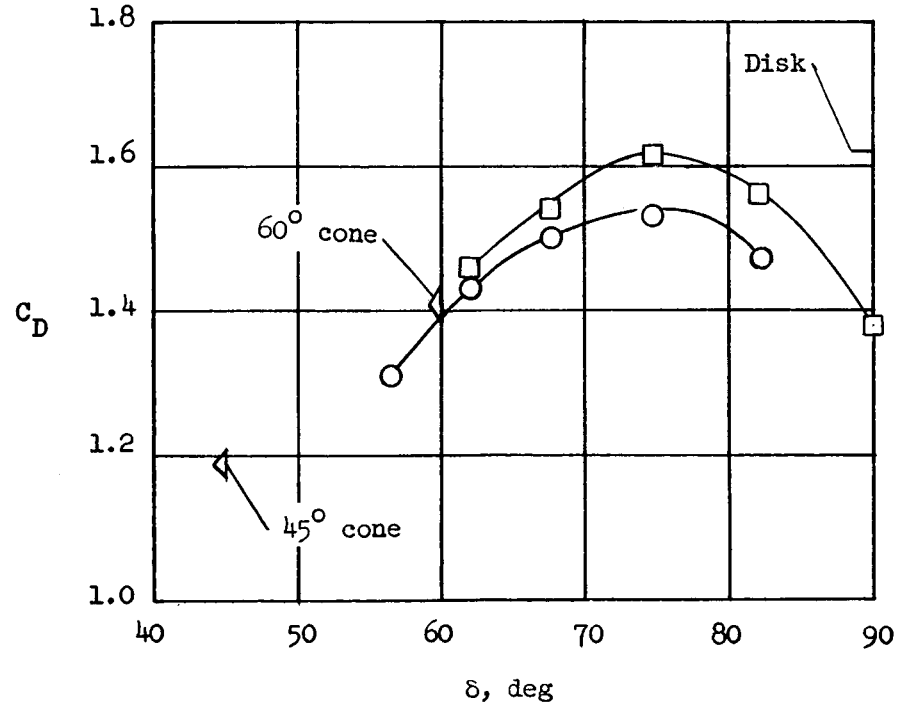

(b) $R \approx 3.0 \times 10^6$.

Figure 13.- Variation of drag coefficient at $\alpha = 0^0$ with flow turning angle for $\frac{r_n}{r_b} = 0.10$ at $M = 3.0$.

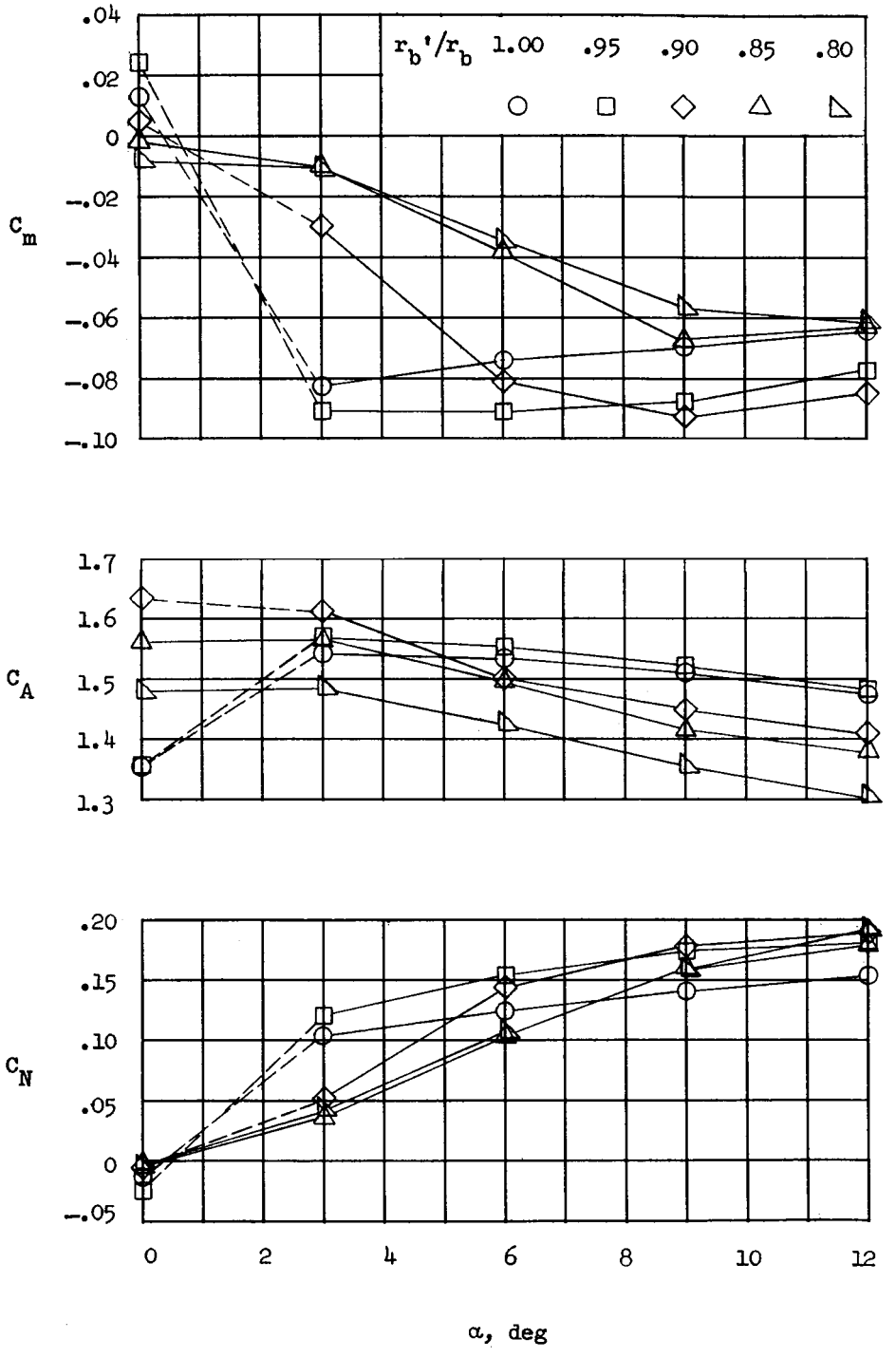

(a) $\frac{r_c}{r_b} = 0$; $R \approx 1.0 \times 10^6$.

Figure 14.- Effects of base radius on longitudinal aerodynamic characteristics for $\frac{r_n}{r_b} = 0.10$ at $M = 3.0$.

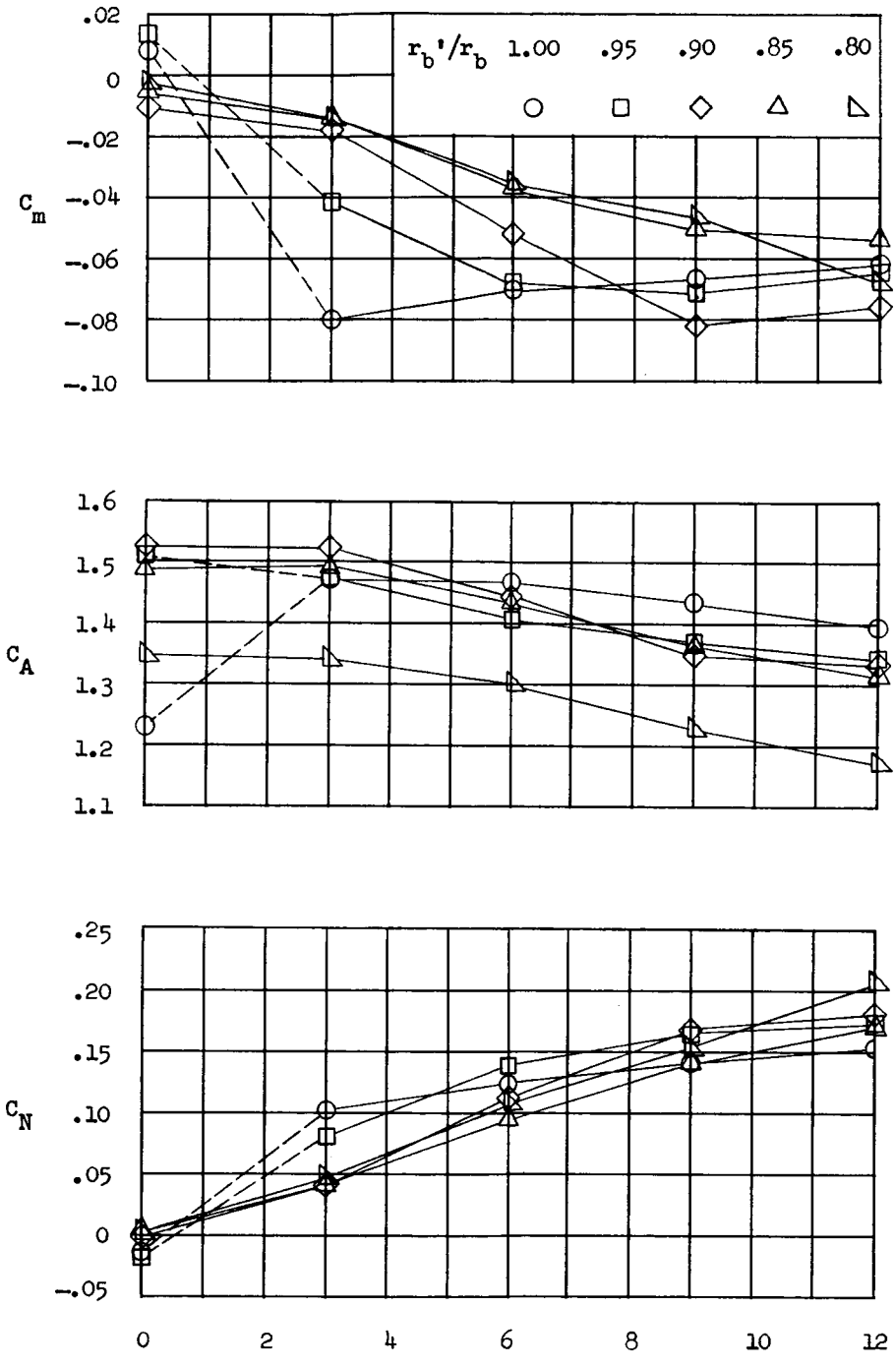

(b) $\frac{r_c}{r_b} = 0.05$; $R \approx 1.0 \times 10^6$.

Figure 14.- Continued.

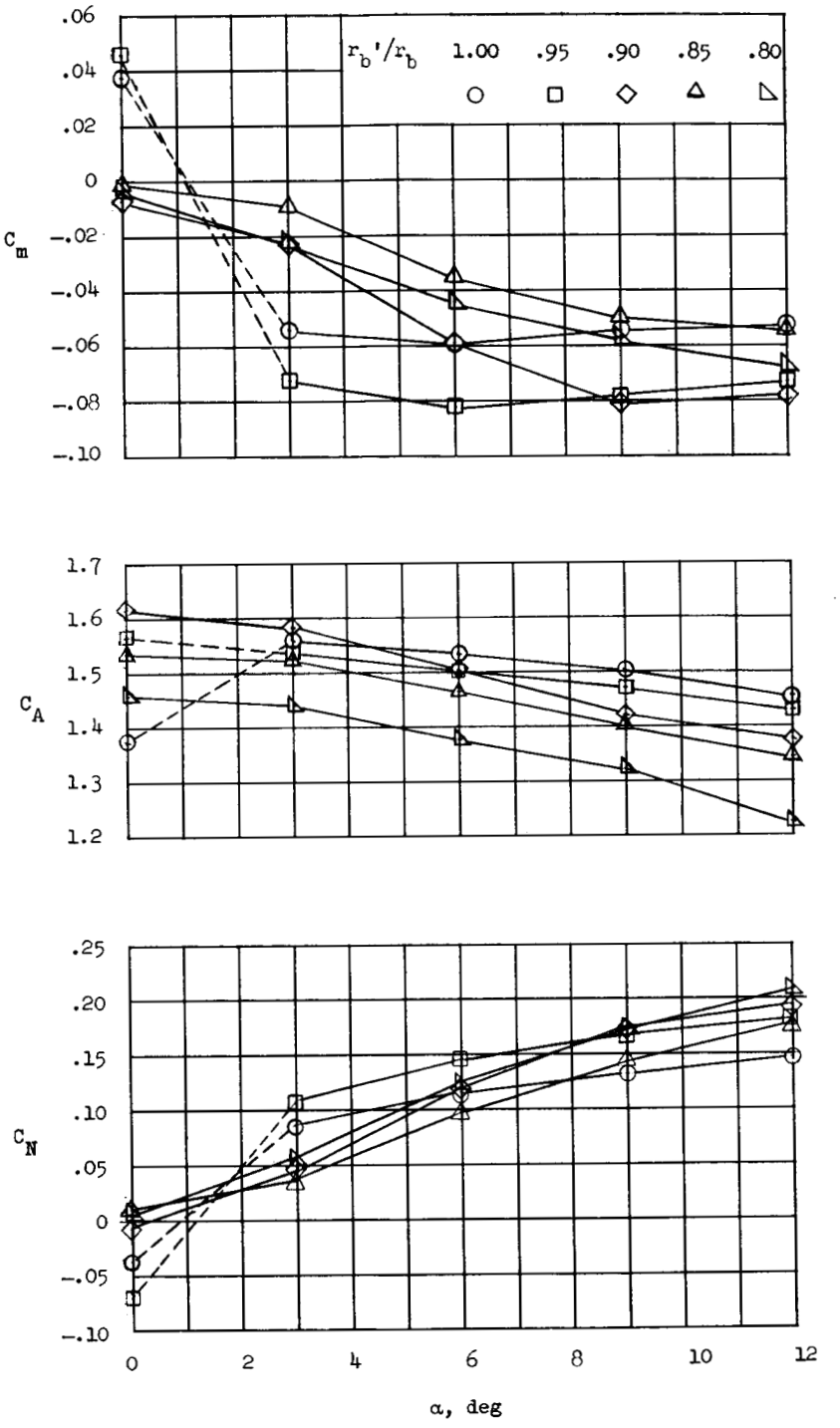

(c) $\frac{r_c}{r_b} = 0$; $R \approx 3.0 \times 10^6$.

Figure 14.- Continued.

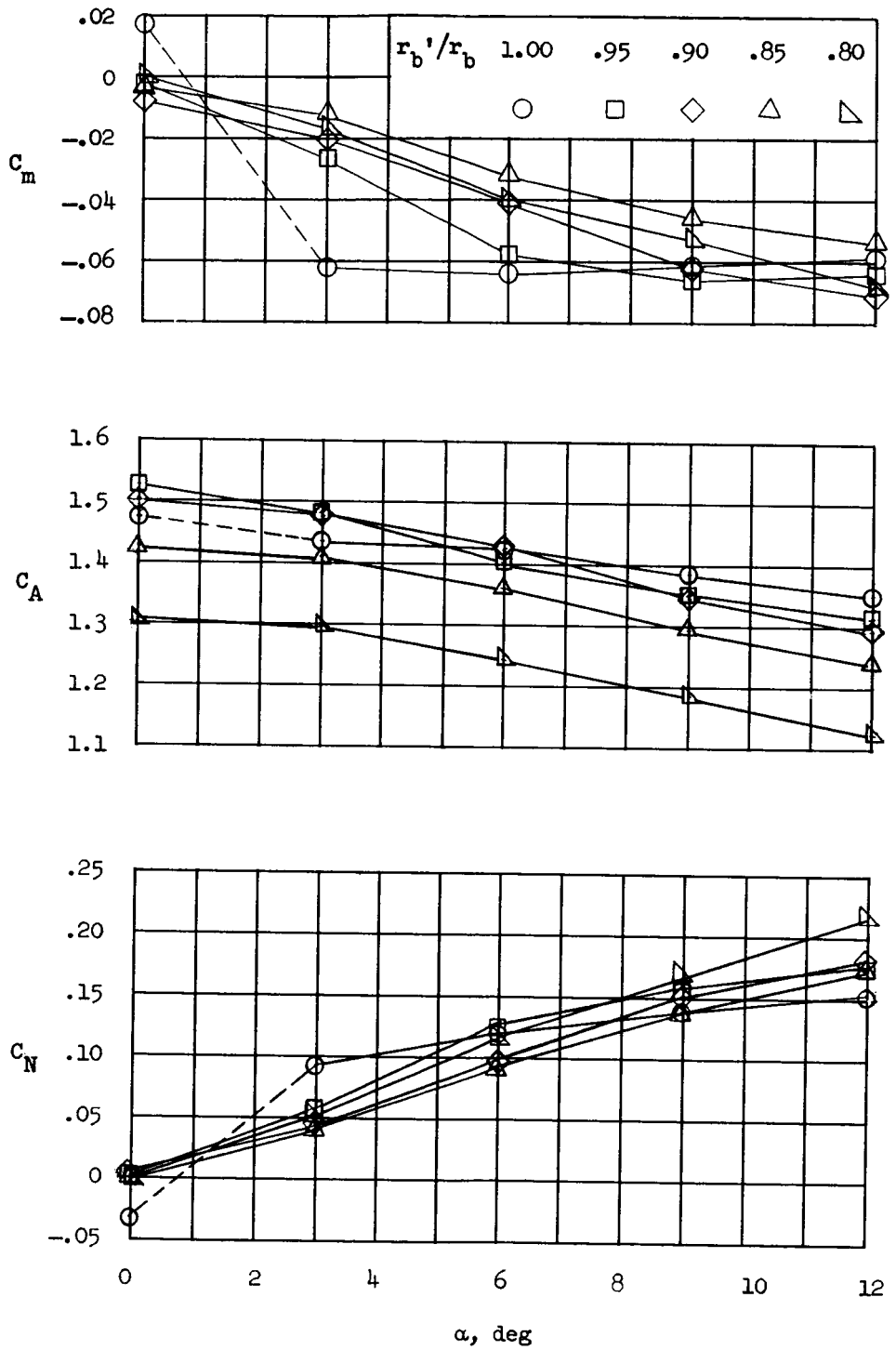

(d) $\frac{r_c}{r_b} = 0.05$; $R \approx 3.0 \times 10^6$.

Figure 14.- Concluded.

8/14/67

"The aeronautical and space activities of the United States shall be conducted so as to contribute . . . to the expansion of human knowledge of phenomena in the atmosphere and space. The Administration shall provide for the widest practicable and appropriate dissemination of information concerning its activities and the results thereof."

—NATIONAL AERONAUTICS AND SPACE ACT OF 1958

NASA SCIENTIFIC AND TECHNICAL PUBLICATIONS

TECHNICAL REPORTS: Scientific and technical information considered important, complete, and a lasting contribution to existing knowledge.

TECHNICAL NOTES: Information less broad in scope but nevertheless of importance as a contribution to existing knowledge.

TECHNICAL MEMORANDUMS: Information receiving limited distribution because of preliminary data, security classification, or other reasons.

CONTRACTOR REPORTS: Scientific and technical information generated under a NASA contract or grant and considered an important contribution to existing knowledge.

TECHNICAL TRANSLATIONS: Information published in a foreign language considered to merit NASA distribution in English.

SPECIAL PUBLICATIONS: Information derived from or of value to NASA activities. Publications include conference proceedings, monographs, data compilations, handbooks, sourcebooks, and special bibliographies.

TECHNOLOGY UTILIZATION PUBLICATIONS: Information on technology used by NASA that may be of particular interest in commercial and other non-aerospace applications. Publications include Tech Briefs, Technology Utilization Reports and Notes, and Technology Surveys.

Details on the availability of these publications may be obtained from:

SCIENTIFIC AND TECHNICAL INFORMATION DIVISION

NATIONAL AERONAUTICS AND SPACE ADMINISTRATION

Washington, D.C. 20546